Title: Alternative splice variants of the mitochondrial fission protein *DNM1L*/Drp1 regulate mitochondrial dynamics and tumor progression in ovarian cancer.

Authors: Zaineb Javed[1,2,3], Dong Hui Shin[3,β], Weihua Pan[1,2], Sierra R. White[2,4], Yeon Soo Kim[3,χ], Amal Taher Elhaw[1,2,3], Shriya Kamlapurkar[1,2], Ya-Yun Cheng[1,2], J Cory Benson[5], Ahmed Emam Abdelnaby[5], Rébécca Phaëton[6,δ], Hong-Gang Wang[7], Shengyu Yang[8], Mara L.G. Sullivan[9], Claudette M. St.Croix[9], Simon C. Watkins[9], Steven J. Mullett[5, 8], Stacy L. Gelhaus[5, 8], Nam Lee[9], Lan G. Coffman[1,2], Katherine M. Aird[1,3], Mohamed Trebak[1,3,4,10], Karthikeyan Mythreye[11], Vonn Walter[12], Nadine Hempel[1,2,4,*]

[1] UPMC Hillman Cancer Center, University of Pittsburgh School of Medicine, PA, USA

[2] Department of Medicine, Division of Hematology/Oncology, University of Pittsburgh School of Medicine, PA, USA

[3] Department of Pharmacology, College of Medicine, Pennsylvania State University, Hershey, PA, USA

[4] Vascular Medicine Institute (VMI), University of Pittsburgh School of Medicine, PA, USA

[5] Department of Pharmacology and Chemical Biology, University of Pittsburgh School of Medicine, PA, USA

[6] Department of Obstetrics & Gynecology, College of Medicine, Pennsylvania State University, Hershey, PA, USA

[7] Department of Pediatrics, College of Medicine, Pennsylvania State University, Hershey, PA, USA

[8] Department of Cellular and Molecular Physiology, College of Medicine, Pennsylvania State University, Hershey, PA, USA

[9] Center for Biologic Imaging, University of Pittsburgh School of Medicine, PA, USA

[8] Health Sciences Mass Spectrometry Core, University of Pittsburgh, PA, USA

[9] Division of Pharmacology, Chemistry and Biochemistry, College of Medicine, University of Arizona, Tucson, AZ, USA

[10] Vascular Medicine Institute (VMI), University of Pittsburgh School of Medicine, PA, USA

[11] Department of Pathology and O'Neal Comprehensive Cancer Center, Heersink School of Medicine, University of Alabama at Birmingham, Birmingham, AL, USA

[12] Department of Public Health Sciences, Division of Biostatistics and Bioinformatics and Department of Biochemistry and Molecular Biology, College of Medicine, Pennsylvania State University, Hershey, PA, USA

***Corresponding Author:**

Nadine Hempel, PhD

University of Pittsburgh School of Medicine, Division of Hematology/Oncology

UPMC Hillman Cancer Center

The Assembly, Rm 2039

5051 Centre Ave, Pittsburgh, PA 15213

Ph: 412-648-4822

nah158@pitt.edu

Current Address:

[β] School of Pharmacy, Virginia Commonwealth University, Richmond, VA, USA

[χ] Division of Human Biology, Fred Hutchinson Cancer Center, Seattle, WA, USA

[δ] GlaxoSmithKline, Collegeville, PA, USA

Abstract

Aberrant mitochondrial fission/fusion dynamics have been reported in cancer cells. While post translational modifications are known regulators of the mitochondrial fission/fusion machinery, we show that alternative splice variants of the fission protein Drp1 (*DNM1L*) have specific and unique roles in cancer, adding to the complexity of mitochondrial fission/fusion regulation in tumor cells. Ovarian cancer specimens express an alternative splice transcript variant of Drp1 lacking exon 16 of the variable domain, and high expression of this splice variant relative to other transcripts is associated with poor patient outcome. Unlike the full-length variant, expression of Drp1 lacking exon 16 leads to decreased association of Drp1 to mitochondrial fission sites, more fused mitochondrial networks, enhanced respiration, and TCA cycle metabolites, and is associated with a more metastatic phenotype *in vitro* and *in vivo*. These pro-tumorigenic effects can also be inhibited by specific siRNA-mediated inhibition of the endogenously expressed transcript lacking exon 16. Moreover, lack of exon 16 abrogates mitochondrial fission in response to pro-apoptotic stimuli and leads to decreased sensitivity to chemotherapeutics. These data emphasize the significance of the pathophysiological consequences of Drp1 alternative splicing and divergent functions of Drp1 splice variants, and strongly warrant consideration of Drp1 splicing in future studies.

Introduction

Mitochondria are highly dynamic organelles continuously undergoing fission and fusion events to facilitate adaptations to cellular and extracellular cues. The opposing processes of mitochondrial fission and fusion are mediated by several evolutionarily conserved dynamin-related GTPases, including Mitofusins (Mfn1&2) and Opa1 which promote fusion, and Dynamin-related Protein 1 (Drp1) which mediates mitochondrial fission [1, 2]. Drp1, which is encoded by the gene *DNM1L*, binds to mitochondrial anchor proteins and forms homo-multimeric helical structures around the outer mitochondrial membrane to initiate division. This process is tightly regulated by Drp1 post-translational modifications [3-7]. Given that the shape of mitochondria are inextricably linked to their function, maintaining a balance between these dynamic fission and fusion events is essential in preserving mitochondrial respiration, and for the proper distribution of mitochondria and mitochondrial DNA during mitosis [8, 9]. Moreover, mitochondrial fission is also an integral component of the apoptotic and mito/autophagy pathways [10, 11]. Perturbation in mitochondrial fission/fusion dynamics have been implicated in cancer, and cancer cells can exploit adaptive mitochondrial dynamics to their advantage to meet their heightened energy demands and to regulate cellular processes including tumor metabolism, stress response pathways and resistance to apoptosis. Several studies have described a role for enhanced fission in cancer [12-14], and this shown to be associated with cell cycle progression [15, 16] and migration [17]. Underlying genetic factors may also contribute to exacerbated signaling that drives the activation of fission, as observed in BRAF and KRAS mutant tumors where Drp1 phosphorylation of S616 is activated via Erk [13, 14, 18]. On the contrary, mitochondrial fission is associated with enhanced apoptosis and thus decreased fission can result in apoptosis resistance [11, 19-21]. Mitochondrial fusion may thus be one mechanism by which tumors evade apoptosis in response to chemotherapeutic agents [22, 23]. These seemingly conflicting studies appear to suggest that both aberrant fission and fusion could have important roles during tumor progression and that the dysregulation of mitochondrial fission and fusion dynamics has the potential to influence various aspects of cancer, including progression, recurrence, and chemoresistance.

In addition to regulation by post-translational mechanisms, alternative splicing of the *DNM1L* pre-mRNA transcript has been shown to give rise to Drp1 splice variants with differential tissue expression, subcellular localization and fission activity [24-29]. Despite the established importance of Drp1 as an integral mitochondrial fission protein few studies have investigated the expression and unique functions of Drp1 splice variants in pathophysiological contexts. While Drp1 has been shown to be overexpressed in several tumor types, the role of

individual splice variants was not considered in these studies. In ovarian cancer *DNM1L* gene amplification has been associated with poor patient outcomes [12, 30]. However, it is unclear how this reflects the relative expression and function of Drp1 splice variants. Here, we show for the first time that transcripts arising from exon 16 splicing are highly expressed in ovarian cancer cells and that relative expression of this transcript to full length Drp1 mRNA is predictive of poor patient outcome. We demonstrate that exon 16 splicing results in a Drp1 protein with a unique function related to regulation of mitochondrial architecture, mitochondrial function, tumor metabolism and chemosensitivity, which is coopted by aggressive ovarian cancer cells, and that relative expression of different Drp1 splice variants has consequences on mitochondrial function and tumor progression. This represents the first study demonstrating the pathophysiological relevance of Drp1 splice variants.

Results

Ovarian cancer cells display distinct Drp1/*DNM1L* splice variant expression.

We previously observed that ovarian cancer cell lines express several different molecular weight protein variants of Drp1 [31]. To determine the clinical significance of this observation, Drp1 protein expression was assessed in ascites-derived epithelial ovarian cancer (EOC) cells isolated from ovarian cancer patients (Fig. 1a). Four bands ranging in molecular weight between ~75-85kDa were detected using a polyclonal antibody raised against the variable and GED domain of Drp1 (Millipore ABT155). Of these, two protein bands were prominently expressed, with propensity for the lower molecular weight band being present in samples of high grade serous ovarian adenocarcinoma origin (HGSA: ECO7, EOC14, EOC15 (Fig. 1a). Two major Drp1 protein bands were also observed in OVCA420 and OVCA433 ovarian cancer cells lines and these validated as being Drp1 using siRNA mediated knock-down (Fig. 1b). Several Drp1/*DNM1L* transcript variants are annotated on the RefSeq record, including alternative splicing of exons 3, 16 and 17 [7, 27, 28, 32, 33]. To determine if the observed Drp1 protein variants are due to alternative start site utilization, splicing or alternate transcriptional termination, 5' and 3' rapid amplification of cDNA ends (RACE) was carried out. 3'RACE revealed that ovarian cancer cells express multiple Drp1 transcripts. This includes mRNAs with alternatively spliced exons 16 and 17, differential 3'UTR lengths, and short transcripts that terminate after exon 14 (ΔC-Ex14) and in intron 17 (ΔC-In17) at predicted alternate polyadenylation sites (Fig. 1c, d and Extended Data Fig. 1a, c). 5'RACE demonstrated utilization of the same transcriptional start site and a splicing out of exon 3 for all transcripts (Extended Data Fig. 1b, c). The ΔC-In17 transcript displayed alternative splicing of exon 16 and

had a predicted alternate stop codon within intron 17, leading to a transcript with a novel coding sequence for 16 amino acids derived from intron 17 (Extended Data Fig. 1c, d). This was predicted to express a 65 kDa protein lacking the C-terminal GED domain (Fig. 1d, e). Using a polyclonal antibody, we were able to detect a protein at the predicted size, which was decreased in expression following siRNA mediate Drp1 knock-down (Extended Data Fig. 1g). This could not be detected when using a monoclonal antibody targeting the C-terminus (Fig. 1b and Extended Data Fig. 1f), suggesting that the ΔC-In17 transcript may result in expression of a truncated protein. ΔC-In17 was detected to variable degrees in other ovarian cancer cell lines and patient derived tumor cells by RT-PCR (Extended Data Fig. 1e, and Extended Data Fig. 3a). Annotation of TCGA ovarian cancer data for the ΔC-In17 transcripts demonstrated that these were detected in <15% of TCGA ovarian cancer specimens (Fig. 2a). While the functional consequences of this novel yet rare C-terminal truncation transcript require further study, we focused on further elucidating the function of alternative splice variants of the variable domain exons 16 and 17 in full length Drp1, as their predicted proteins molecular weights matched the predominant protein variants observed in patient ascites derived EOCs (Fig. 1a, b). Exons 16 and 17 are located in the variable B-domain of Drp1 (Fig. 1e) and alternative splicing of these exons (denoted as 16/17) was further examined using RT-PCR with primers flanking the variable domain. Variable expression of splice variants was found in a panel of ovarian cancer cell lines (Fig. 1f), with the HGSA cell lines OVCAR3, OVCA420 and OVCA433 demonstrating higher relative expression of the transcript with spliced-out exon 16, referred here after as Drp1(-/17).

Patient ascites derived epithelial ovarian cancer cells and tumor specimens display high expression of Drp1 transcript variants lacking exon 16, which is associated with poor patient outcome.

By annotating TCGA RNA sequencing data for the identified Drp1/*DNM1L* transcripts we found that all variable domain (Exons 16 and 17) splice variants of the full-length transcripts were expressed in Ovarian Serous Cystadenocarcinoma TCGA specimens at different levels (Fig. 2a, b). Of the four variable domain variants, highest expression of Drp1(-/17), the transcript lacking exon 16, was observed, followed by Drp1(16/17) and Drp1(-/-) displaying approximately equal expression (Fig. 2b). Drp1(16/-), the transcript lacking exon 17, was least abundant. Similar to our findings in cell lines, most Drp1/*DNM1L* transcripts in TCGA specimens lacked exon 3 (Extended Data Fig. 2a), agreeing with previous work describing exon 3 retention to be predominant in neuronal tissues [27]. TCGA data were independently validated by assessing

splice variant transcript abundance in EOCs isolated from patient ascites (Fig. 2c) and in a separate cohort of matched normal fallopian and omental or ovarian tumor specimens (Fig. 2d). Ascites-derived EOCs classified as HGSA and carcinosarcoma demonstrated predominant expression of the splice variant lacking exon 16, Drp1(-/17), and transcripts containing both exons 16 and 17, Drp1(16/17). In addition, an increase in relative Drp1(-/17) expression was observed in ovarian tumors (11/13 specimens) and omental tumors (5/5) compared to matched benign/normal fallopian tube (Fig. 2d; Extended Data Fig. 3). These data demonstrate that ovarian cancer cells express several Drp1/*DNM1L* splice variants, with a high abundance of Drp1(-/17) expression, and suggest that splicing of exon 16 and retention of exon 17 might be of significance to ovarian cancer.

We were curious if predominance of Drp1 splice variant expression is predictive of patient outcome. While patients with high expression of Drp1(-/17) trended towards worse overall survival (Fig. 2e), comparisons between high and low expression of individual Drp1 splice variants was not able to significantly predict overall survival (Extended Data Fig. 2b). However, grouping patients into mutually exclusive high vs low expression of splice variant pairs based on median expression cut-offs, revealed that relative abundance of the different variable domain splice variants influenced patient outcome (Fig. 2f; Extended Data Fig. 2c, d). Patients with tumors displaying high Drp1(-/17) and low Drp1(16/17) expression demonstrated poor overall survival compared to those with high Drp1(16/17) and low Drp1(-/17) expression (HR: 1.81, 95% CI: 1.076 to 3.071, log rank p=0.0208), with a median survival difference of 14.3 months (Fig. 2f). High Drp1(-/17):low Drp1(16/-) expression also decreased median survival by 11.7 months, albeit not significantly (HR: 1.508, 95% CI: 0.9304 to 2.444, log rank p=0.088). Other mutually exclusive expression comparisons between Drp1 splice variants were not significantly predictive of survival (Extended Data Fig. 2d). Although Drp1(16/17) and Drp1(-/17) transcript variants are both abundant in ovarian cancer cell lines and patient specimens, the above data suggest that their relative expression has consequences on ovarian cancer progression. Yet, the significance of exon 16 splicing on Drp1 function had now previously been explored in cancer.

Loss of Exon 16 abrogates association with mitochondrial fission puncta and leads to more fused mitochondrial networks.

The HGSA OVCA433 cell lines was chosen as a model for subsequent studies as it displayed similar *DNM1L* variable domain transcript expression as HGSA patient specimens, while SKOV3 cells were chosen as a model due to their relatively equal expression of all four

full length variable domain variants. To investigate their function, Drp1 splice variants were expressed as GFP fusion proteins by lentiviral transduction in both cell lines (Fig. 3a and Extended Data Fig. 4a). Drp1(16/17) which contains exons 16 and 17 was localized to the cytosol and at distinct mitochondrial fission puncta, as previously described by numerous Drp1 overexpression studies [6, 27, 34]. On the contrary, Drp1(-/17) displayed less mitochondrial association and fewer aggregation into fission puncta. Instead, Drp1(-/17) exhibited a filamentous pattern of localization (Fig. 3b). Consistent with the work by Strack and Cribbs, who demonstrated that the splicing of exon 16 modifies the association of Drp1 with mitochondria and increases binding to microtubules [27], we found that Drp1(-/17) exhibited overlapping staining with tubulin in ovarian cancer cells (Fig. 3b,c and extended Data Fig. 4b,c).

The expression of Drp1(-/17) was previously reported to lead to more fused and elongated mitochondrial network, likely due to the reduced association of Drp1(-/17) with mitochondria [27]. In line with this, compared to both GFP control and Drp1(16/17), cells expressing Drp1(-/17) had longer average mitochondrial branch lengths and a greater number of branches per mitochondria, indicative of a more interconnected mitochondrial network (Fig. 3d, and extended data Fig. 4d). In contrast, expression of Drp1(16/17) led to shorter branch lengths and fewer branches per mitochondria, a predicted phenotype following overexpression of Drp1 (Fig. 3d, Extended Data 4&5). TEM imaging additionally demonstrated elongated mitochondrial phenotypes in Drp1(-/17) expressing cells, contrasting with the smaller, more circular mitochondria seen following expression of Drp1(16/17) (Fig. 3e, f and Extended Data Fig. 4e and 5). Notably, expression of Drp1(-/17) led to an overall higher number and density of cristae per mitochondria (Fig. 3e, f and Extended Data Fig. 5). These observations suggest that high expression of Drp1(-/17) could lead to abrogated mitochondrial fission and a more fused mitochondrial network, likely due to decreased association with mitochondrial fission puncta and partial localization to microtubules. Moreover, after exposure to the pro-fission stimulus FCCP Drp1(-/17) did not associate with mitochondrial fission puncta, unlike Drp1(16/17). Instead, Drp1(-/17) continued to exhibit high association with the microtubule network and mitochondria maintained their elongated mitochondrial morphology (Extended Data Fig. 6). This suggests that cells expressing Drp1(-/17) have reduced response to pro-fission stimuli. These findings are significant, as Drp1 splice variants display clear differences in localization and function as fission proteins, yet past studies have primarily investigated the function of Drp1 in cancer cells by overexpressing the Drp1(16/17) transcript that includes both exons 16 and 17. Thus, we next investigated the functional consequences of Drp1(-/17) expression in ovarian cancer cells.

Expression of Drp1(-/17) increases oxygen consumption and alters tumor cell metabolism.

Due to their continuous membranes and matrix lumens, fused mitochondrial networks can facilitate better diffusion of molecules, including ADP, and reducing equivalents NADH and FADH2, necessary for oxidative phosphorylation [35, 36]. In addition, a more ordered cristae architecture improves electron transport chain super complex assembly, and these structural features have been associated with optimal mitochondrial respiration [37-39]. Given that Drp1(-/17) splice variant expression leads to enhanced mitochondrial networks and cristae numbers the effects on mitochondrial respiration and cellular metabolism were assessed. Using extracellular flux analysis significant increases in basal oxygen consumption rates (OCR), ATP-dependent OCR and spare respiratory reserve were observed between Drp1(-/17) and Drp1(16/17) expressing OVCA433 cells (Fig. 4a, b). An increase in OCR was similarly observed in SKOV3 cells expressing Drp1(-/17) (Extended Data Fig. 7a, b). There were no differences in the expression of mitochondrial proteins COX-I (complex IV), and SDH-A (Complex II) following expression of either Drp1 variant suggesting that changes in mitochondrial activity are likely not attributable to changes in mitochondrial biogenesis (Extended Data Fig. 8a, b). In addition, no consistent changes in mitochondrial membrane potential or significant changes in mitoSox fluorescence, an indicator of mitochondrial oxidant production, were associated with the expression of either Drp1 variant in the cell lines tested (Extended Data Fig. 8c, d).

Compared to Drp1(16/17) or GFP controls, untargeted metabolomics (Fig. 4c) showed that cells expressing Drp1(-/17) also display an increase in metabolites linked to glycolysis and the pentose phosphate pathway. Related to the observed increases in lactate levels, an increase in extracellular acidification rate was also seen, although this was not significant in OVCA433 cells (Extended Data Fig. 7c-f). Select metabolites necessary for *de novo* purine and pyrimidine synthesis, such ribulose-5-phosphate, glycine and aspartate, and most TCA cycle metabolites were also elevated following overexpression of Drp1(-/17) relative to GFP control and Drp1(16/17) (Fig. 4c). These changes were accompanied by elevated total NAD(H) levels and a decrease in the NAD+/NADH ratio (Fig. 4d and Extended Data Fig. 7g), which may be contributing to the reducing equivalents necessary for increased respiration seen in Drp1(-/17) cells. Collectively, these findings suggest that enhanced Drp1(-/17) expression leads to an energetic phenotype and alters metabolism of ovarian cancer cells compared to cells expressing Drp1(16/17).

Drp1 splice variant expression differentially affects tumorigenicity.

DNM1L gene amplification has been reported to correlate with cell cycle gene expression and poor patient outcomes in chemoresistant and recurrent ovarian cancer cases [12]. However, previous work did not account for expression of specific Drp1 splice variants, and it is thus unknown which Drp1 transcript variant is specifically associated with this pro-tumorigenic phenotype. Considering that high Drp1(-/17) relative to low Drp1(16/17) expression is associated with lower overall patient survival (Fig. 2f), we further assessed the impact of Drp1 variable domain splice variant expression on tumor cell behavior. Drp1(-/17) expression significantly increased the proliferation rate of both SKOV3 and OVCA433 cells, compared to GFP control and Drp1(16/17) (Fig. 5a), and Drp1(16/17) expression significantly decreased clonogenic survival (Fig. 5b). In addition, cells expressing Drp1(-/17) also exhibited a significant increase in migration compared to GFP and Drp1(16/17) expressing cells (Fig. 5c). An intraperitoneal tumor xenograft model demonstrated that expression of Drp1(-/17) and Drp1(16/17) influences the location and degree of tumor burden in the peritoneal cavity (Fig. 5d-e). Overall, cells expressing Drp1(16/17) displayed delayed onset of tumor growth and the lowest overall tumor burden within the peritoneal cavity (Fig. 5d-g), correlating with our observations in cell culture. Mice injected with GFP-control expressing SKOV3 cells reached endpoint first, with tumor burden largely localized to the peritoneal wall near the IP injection site (Fig. 5e). In contrast, mice injected with Drp1(-/17) cells developed tumors primarily in the omentum, a major site of ovarian cancer metastatic spread in the abdominal cavity (Fig. 5f). Omental tumors also differed morphologically, with cells expressing Drp1(-/17) forming a greater number of smaller and denser multi-lobular lesions along the omentum and displacing most of the omental adipocytes (Fig. 5g). Taken together, these data show for the first time that Drp1 splice variants differentially influence proliferation, migration and *in vivo* tumor growth of cancer cells, and that expression of Drp1(-/17) is advantageous to omental tumor progression.

Drp1(-/17) protects cells against chemotherapy induced apoptosis.

Previous findings suggest the involvement of mitochondrial fission in the initiation of apoptosis[11, 19, 40], and thus decreased fission has been proposed as a mechanism of apoptosis resistance in cancer cells. Interestingly, Drp1(-/17) expression was shown to abrogate staurosporin-mediated cell death of astrocytes in cell culture[27]. We thus sought to test if high expression of Drp1(-/17) and the concomitant increase in fused mitochondria may be beneficial to tumor cells when challenged with cisplatin or paclitaxel treatment (Fig. 6a). Expression of Drp1(-/17) led to a statistically significant increase in IC50 values for both compounds in OVCA433 and SKOV3 cells relative to GFP controls (Fig. 6b). Conversely, Drp1(16/17)

expression enhanced cell death in response to both compounds compared to GFP control cells, which was particularly evident with Cisplatin (Fig. 6a, b). Notably, cells with Drp1(16/17) expression exhibited the highest caspase 3/7 activity in response to both agents (Fig. 6c), while Drp1(-/17) expression significantly abrogated caspase activity relative to GFP and Drp1(16/17) expressing cells following cisplatin and paclitaxel treatment. These data suggest that Drp1(16/17) mediated mitochondrial fission enhances apoptosis of ovarian cancer cells, and that Drp1(-/17), which abrogates mitochondrial fission, protects cells from apoptosis. To determine if Drp1 splice variants differ in activation by post-translational modifications in response to chemotherapeutic agents, phosphorylation of Serine 616 was investigated. Although predominantly observed in OVCA433 cells, Drp1(16/17) was more susceptible to phosphorylation at S616 upon treatment with both cisplatin and paclitaxel, while no change in phosphorylation was observed in Drp1(-/17) in response to these agents (Extended data Fig. 9). Finally, the effects of Cisplatin on *in vivo* tumor growth were tested using a subcutaneous xenograft model (Fig. 6e). In the saline treated groups Drp1(-/17) expression significantly increased final tumor volume of subcutaneous tumors compared to both GFP and Drp1(16/17) expressing SKOV3 cells when mice were euthanized at the same endpoint (Fig. 6d). Similar to observations in the omentum, subcutaneous tumors from Drp1(-/17) expressing cells were multi-lobular. In addition, mice injected with Drp1(-/17) expressing cells developed lymph node lesions (Fig. 6d), again suggesting that expression of Drp1(-/17) enhances the metastatic behavior of cells. In the cisplatin treated groups, none of the GFP and Drp1(-/17) expressing tumors responded to cisplatin treatment and all progressed after cisplatin removal. On the contrary, 4/10 Drp1(16/17) expressing tumors either completely responded or did not reach a tumor volume threshold of 200mm^3 at study endpoint (Fig. 6e, f), validating cell culture studies that Drp1(16/17) expression leads to higher chemosensitivity. Although final Drp1(-/17) tumor weights at endpoint were lower than GFP controls in the cisplatin treated groups, Drp1(-/17) tumors again displayed gross differences and a more metastatic phenotype. Drp1(-/17) subcutaneous tumors were multilobular and were the only tumors that developed lymph node lesions under treatment with cisplatin (Extended data Fig. 10). Altogether, these data demonstrate that the loss of exon 16 through alternative splicing influences the role of Drp1 in tumor cells, leading to changes in metastatic and chemoresistance phenotypes of cancer cells.

Manipulation of endogenous Drp1 splice variant ratios can dictate the pro-tumorigenic function of Drp1(-/17).

The data above clearly show that expression of Drp1(-/17), the splice variant lacking exon 16, has significantly different effects on mitochondrial morphology and function, tumor cell behavior, and chemosensitivity compared to expression of the full length Drp1(16/17). To rule out that these observations are due to overexpression of recombinant protein, we sought to assess whether altering the endogenous ratios of Drp1 splice variants could elicit similar effects. To achieve this, splice variant-specific siRNAs targeting each of the four endogenous variable domain Drp1/*DNM1L* splice variants were designed (Fig. 7a, b). SKOV3 cells were used as a model for these experiments, as this cell line displays relatively equal expression of the four variable domain Drp1 transcript variants (Fig. 7a), thus allowing us to tune the ratios of their relative expression using siRNAs. Specific knock-down of individual splice variants transcripts (Fig. 7a) led to altered Drp1 protein variant expression (Fig. 7b). While it was more difficult to resolve Drp1(16/17) and Drp1(16/-) on SDS-PAGE due to their close molecular weight individual knockdowns of Drp1 protein variants could be distinctly visualized (Fig. 7b). A positive control siRNA designed to target Exon 15 led to decreased protein expression of all variants (Fig. 7b, lane 2). The knock-down of all variants (siDrp1 total) resulted in fused mitochondrial morphology as expected, and as demonstrated by previous studies targeting Drp1 by RNAi [41-43] (Fig. 7c,d). When targeting specific Drp1 splice variants with siRNA, we observed varying degrees of impact on mitochondrial networks (Fig. 7c, d and Extended Data Fig. 11a, b). Drp1(16/17) knockdown most closely replicated the highly elongated mitochondrial morphology and increased branching seen with total Drp1 knockdown (siDrp1-total, Fig. 7c, d). In contrast, with knockdown of Drp1(-/17) these effects were muted (Fig. 7c, d), again highlighting that Drp1(-/17) contributes less to mitochondrial fission than Drp1(16/17). The combination knockdown of Drp1(-/16) and Drp1(-/-), which essentially enriches for higher but equal expression of Drp1(16/17) and Drp1(-/17), led to an intermediary increase in mitochondrial length and branching (Fig. 7c, d). This suggests that the endogenous ratio of expression between the Drp1(16/17) and Drp1(-/17) splice variants is critical in determining the overall fission activity of Drp1. Collectively, these results confirm our overexpression data (Fig. 3), suggesting that the Drp1(16/17) variant plays a more active role in mitochondrial fission, while Drp1(-/17) contributes less to mitochondrial fission.

Importantly, the functional consequences of altered Drp1 splice variants expression on mitochondrial function could similarly be recapitulated using siRNA to target endogenous Drp1 transcripts. By recombinant expression we showed that Drp1(16/17) was detrimental to mitochondrial respiratory function while Drp1(-/17) expression improved OCR (Fig. 4 and Extended Data Fig. 7). In agreement with this, inhibition of Drp1(16/17) improved respiration

while siRNA targeting of Drp1(-/17) decreased both basal and ATP-linked oxygen consumption rate (OCR) (Fig. 8a, b). No significant changes in mitochondrial function were observed upon combined knockdown of Drp1(16/-) and Drp1(-/-) which enrich for equal expression of Drp1(16/17) and Drp1(-/17) (Fig. 8c). These data again suggest that an imbalance of Drp1(16/17) and Drp1(-/17) expression is necessary to drive changes in mitochondrial function.

Subsequently, we investigated the changes in cellular proliferation and migration upon perturbation of endogenous Drp1 variants (Fig. 8d, e, f). Total knockdown of all Drp1 transcripts (siDrp1-total) drastically reduced both cellular proliferation and migration. Compellingly, increased cellular proliferation was only seen when Drp1(16/17) was knocked down, or when specific enrichment of Drp1(-/17) was achieved by a combined knockdown of the other three variable domain variants (siDrp1(16/17),(-/16) and (-/-); Fig. 8e). These conditions mimic Drp1(-/17) overexpression (Fig. 5b) and mirror the low Drp1(16/17):high Drp1(-/17) expression observed in the TCGA patient cohort that is marked by poor overall survival (Fig. 2f). Similarly, cell migration was enhanced following knockdown of Drp1(16/17), and significantly decreased after knockdown of Drp1(-/17) (Fig. 8f; Extended Data Fig. 11). Thus shifting endogenous expression to high Drp1(-/17):low Drp1(16/17) ratios using siRNA validates the pro-proliferative and migratory phenotypes observed by Drp1(-/17) variant overexpression. The above findings also emphasize the importance of the expression ratio between the Drp1(16/17) and Drp1(-/17) variants. This is demonstrated by the observation that a combined knockdown of Drp1(-/16) and Drp1(-/-), reflecting an equal enrichment of expression of both Drp1(16/17) and Drp1(-/17), led to relatively minor changes in mitochondrial morphology, with no significant impact on mitochondrial function, cellular proliferation or migration. Taken together, these data emphasize that changes in the ratio of Drp1 splice variant expression can have profound effects on mitochondrial morphology and metabolism that have consequences on tumor cell function.

Discussion

To our knowledge this is the first description of Drp1/*DNM1L* transcript variants and their functional significance in a pathophysiological setting. While Drp1 has been extensively studied in various diseases, including multiple cancers [12, 14, 44-46], the investigation of different Drp1 isoforms arising from alternative splicing has remained limited, with few studies conducting direct comparisons [26, 27, 29, 32, 47]. Moreover, prior research has often neglected to specify which Drp1 isoform was the subject of study. It is assumed that most prior works utilized plasmid that contain all exons of the variable domain (i.e., Drp1(16/17)) to overexpress recombinant Drp1, or that knock-down strategies targeted the expression of all Drp1 variants. Our findings demonstrate that alternative splicing of exon 16 is an important feature of ovarian cancer, that this is associated with poor patient outcome, and that alternative splicing of exon 16 results in expression of 2 *DNM1L*/Drp1 proteins with distinct function related to regulation of mitochondrial form and function. Thus, our work strongly supports that future studies focused on Drp1 should take expression and function of *DNM1L*/Drp1 splice variants into consideration.

According to TCGA data the *DNM1L* gene is amplified in >50% serous ovarian cancer cases (5% high level amplification, 46% low level gain), while only 7% of cases show heterozygous loss (Extended Data Fig.2e). Published work has correlated *DNM1L* amplification with enhanced cell cycle gene expression and poor survival in chemo-resistant and recurrent cancer samples [12, 30]. Notably, previous analyses of mRNA expression did not discern levels of specific Drp1 splice variants, leaving it uncertain which transcripts are associated with cell cycle gene expression, prognosis, and chemoresistance. We found that ovarian cancer cells derived from patient ascites, as well as TCGA ovarian cancer specimens express high levels of the transcript lacking exon 16 [Drp1(-/17)]. Strikingly, high Drp1(-/17) expression relative to Drp1(16/17) correlates with poorer overall patient survival. The identification that a specific Drp1 splice variant is linked to unfavorable patient outcome underscores the clinical impact of Drp1 splice variant expression in cancer for the first time.

We established that the two major ovarian cancer Drp1 splice variants, Drp1(-/17) and Drp1(16/17) have distinct localization and effects on mitochondrial morphology and function. The Drp1(-/17) alternative splice variant was previously reported to localize to microtubules[27]. Similarly, compared to Drp1(16/17) we observed that Drp1(-/17) associated more frequently with microtubules rather than mitochondria, and this likely explains why Drp1(-/17) expression shifts mitochondrial morphology towards a fused state. Importantly, through splice-site specific knockdown of Drp1 variants, we provide the first validation of the fusion phenotype associated with Drp1(-/17) at endogenous expression levels. The variant specific knockdowns also

emphasize the significance of stoichiometric expression of the Drp1 splice variants in fine tuning regulation of mitochondrial morphology, possibly representing a novel mechanism exploited by cancer cells to manipulate their mitochondrial dynamics and subsequently mitochondrial function.

Decreased fission, and a consequentially more fused mitochondrial network has been shown to enhance electron transport chain super-complex assembly and to improve mitochondrial respiratory function[39, 48]. We demonstrated that Drp1(-/17) expression is associated with enhanced mitochondrial respiratory function and more compact cristae arrangement potentially enabling cancer cells to thrive under stress when heightened mitochondrial function is necessary. Stress-induced mitochondrial hyperfusion has been shown to confer stress resistance and to promote cell survival[35, 49, 50]. Similarly, the fused networks resulting from elevated Drp1(-/17) expression likely allow ovarian cancer cells to bolster mitochondria robustness and maintain metabolic efficiency. Cells expressing Drp1(-/17) display a more active metabolic phenotype, characterized by elevated respiration, glycolysis and TCA cycle metabolites. Numerous studies have emphasized the significance of dynamically adapting mitochondrial morphology to drive metabolic flexibility and regulate cell survival [35, 49-53]. The preference for metabolic fuels is also closely associated with mitochondrial architecture[53-55]. The reliance of tumor cells on manipulating their mitochondrial respiration and function is highlighted by numerous recent studies[56, 57]. Ovarian cancer stem cells and chemoresistant cells exhibit a remarkably adaptable metabolic phenotype, capable of switching between glycolysis and oxidative phosphorylation depending on which pathway confers a selective growth advantage and chemoresistance[31, 35, 52, 56, 58-60]. Moreover, metabolic alterations are essential to sustain unbridled growth in cancer cells, with increased ATP synthesis and a shift towards de novo macromolecule biosynthesis. While the increased mitochondrial networking observed in Drp1 (-/17) and cristae architecture potentially contributes to ETC complex assembly and efficiency in oxidative phosphorylation, the observed increase in TCA cycle metabolites is also suggestive of an increase in TCA cycle flux, which could be driven by the need for NADH reducing equivalents, as demonstrated by increased levels of NADH in Drp1(-/17) cells. It remains to be determined if mitochondrial architecture also contributes to the activity or efficiency of TCA cycle enzymes, although it is known that substrate availability is enhanced by a more fused mitochondrial network [36, 39].

Prior metabolic profiling of ovarian cancer cells and tumors derived from patients has revealed discernible differences in purine and pyrimidine metabolism, glycerolipid metabolism, and energy metabolism [59, 61, 62]. Interestingly, akin to these observations, Drp1(-/17) expression

correlated with heightened levels of amino acids like glutamine, glycine, and aspartate, all crucial components for purine and pyrimidine metabolism. Furthermore, the decreased serine levels and increased glycine levels associated with Drp1(-/17) expression suggest enhanced catabolism of the nonessential amino acid serine through one-carbon metabolism, essential for purine nucleotide synthesis. It remains to be determined if the expression of Drp1(-/17) and the concomitant improved mitochondrial function thus grants ovarian cancer cells greater metabolic flexibility and confers survival advantages in the face of shifting nutrient availability, or if expression of specific Drp1 splice variants can lead to metabolic vulnerabilities that could be harnessed for therapeutic intervention.

Drp1 has been extensively studied as a regulator of cell death and proliferation. Drp1-mediated fission has been shown to be crucial for mitosis in cancer cells[14, 15]. Yet it is known that during G1-S transition, mitochondrial networks fuse, which aids in cyclin E mediated G1-S transition, and inhibition of Drp1-mediated fission can induce the proliferation of quiescent cells [63]. Similarly, elevated mitochondrial fusion has been identified as a feature of ovarian cancer neoplastic stem cells, priming them for self-renewal and proliferation [64]. Our present work suggests distinct impacts of Drp1 alternative splice variants on cell proliferation, and one might speculate that their variable abundance could be associated with changes in cell cycle progression. Moreover, the association of Drp1(-/17) with microtubules has been related to phosphorylation by cyclin dependent kinases, where Cdk1 leads to Drp1(-/17) microtubule dissociation, while CDK5 mediates microtubule association of Drp1(-/17) during interphase [27].

Another significant observation is that Drp1 splice variants alter the chemosensitivity of ovarian cancer cells. Improved mitochondrial function and increased oxidative phosphorylation, as seen in ovarian cancer cells with Drp1(-/17) splice variant expression, are established phenotypes of chemoresistance development in tumor cells, including ovarian cancer [65, 66]. This has led the way for targeting OxPhos therapeutically. Moreover, since mitochondrial fission is an essential process during apoptosis [11, 19-23], the increased fused mitochondrial networks in Drp1(-/17) expressing cells may further account for the observed resistance to apoptosis upon exposure to agents like cisplatin and paclitaxel. As such, previous studies have reported higher abundance of tubular and elongated mitochondria in chemoresistant ovarian cancer cells[67, 68]. We propose that heightened resistance to chemotherapy, coupled with the survival advantages conferred by improved mitochondrial function, contribute to the poor outcome observed in patients with high tumor expression of Drp1(-/17).

Given the unique association of Drp1(-/17) with microtubules, the target site of taxanes, further investigations are warranted to ascertain whether the heightened chemoresistance

conferred by Drp1(-/17) is attributed to reduced mitochondrial fission or its interaction with microtubules. The interaction of Drp1 with microtubules was previously shown to be driven by direct, electrostatic interactions between the conserved basic residues in Drp1 exon 17 (Arg566/567) and the acidic N-termini of α/β-tubulin. The existence of exon 16 in the Drp1(16/17) sequence is hypothesized to impede this interaction, possibly by physically obscuring or neutralizing the positive charge of the neighboring microtubule binding domain [27]. Future work is needed to elucidate potential extra mitochondrial function of Drp1(-/17) and how these could be additionally contributing not only to the abrogated fission activity of this protein, but other cellular functions that play a role in driving the enhanced tumorigenic features of cells predominantly expressing this variant.

While our work focused on ovarian cancer, the importance of Drp1 splice variants in other tumor types requires further investigation. Other shortcomings of this work that require further investigation are the lack of understanding as to why and how exon 16 is specifically spliced out in ovarian cancer cells. Cancer cells in general are known for their alterations in RNA splicing and processing [47, 69, 70] and it remains to be determined if specific alterations in the RNAs splicing machinery give rise to higher expression of Drp1(-/17). As such, aberrant expression of RNA splice factors such as SRSF3 is associated with ovarian cancer [71, 72].

In summary, our study sheds light on the pathophysiological importance of Drp1 variant expression and their ability to modify mitochondrial fission and fusion dynamics as a novel mechanism underlying ovarian cancer cell plasticity. This study also emphasizes the necessity of expanding our comprehension of these Drp1 splice variants, potentially beyond the scope of cancer, and their consideration in future investigations on the function of Drp1 in different (patho)physiological settings.

Materials & Methods

Cell lines and cell culture

Cell lines were generously provided by the following investigators: OVCA433, OVCA420 Dr. Susan K. Murphy; HeyA8, Dr. Katherine Aird; FT282, Dr. Ronny Drapkin. ES-2, TOV-21-G and OVCAR3 cells were purchased from American Type Culture Collection (ATCC, CRL-1978, HTB-161). OVCA433, OVCA420, SKOV3 and HeyA8 cells were cultured in RPMI 1640 medium (Corning,10-040-CV) supplemented with 10% fetal bovine serum, FBS (Avantor® Seradigm,1500-500). OVCA433 and SKOV3 cells under selection were maintained in fully supplemented growth media with 5ug/ml Puromycin (Gibco™, A1113803). OVCAR3 cells were cultured in RPMI1640 medium supplemented with 0.01 mg/ml bovine insulin (Fisher Scientific,50-

608-896) and 10% FBS ES-2 cells were cultured in Modified McCoy's 5a Medium (Corning,10-050-CV) with 10% FBS. TOV-21-G cells were cultured in a 1:1 mix of MCDB 105 (Sigma-Aldrich,117-500) containing 1.5 g/L sodium bicarbonate (Gibco™,25080094) and Medium 199 (Corning,10-060-CV) containing 2.2 g/L sodium bicarbonate, with 15% FBS. FT282 cells were cultured in 50% DMEM and 50% Ham's F-12 medium (Corning,10-090-CV) supplemented with 2% FBS. All cells were maintained at 37°C with 5% CO_2. Cell lines were routinely tested for Mycoplasma contamination using EZ-PCR™ Mycoplasma Detection Kit (Captivate Bio,20-700-20). Cell line authentication was carried by STR genotyping (Labcorp).

Patient ascites derived EOC cells.

Epithelial Ovarian Cancer (EOC) cells were isolated from malignant ascites of ovarian cancer patients treated at the Women's Cancer Care clinic (Albany, NY) and the Penn State Hershey College of Medicine Division of Gynecologic Oncology, with approval granted from the State University of New York at Albany and the Penn State College of Medicine IRBs. Histological subtype and staging of EOC samples shown in Fig. 2c. Following procurement of ascites EOCs were immediately isolated and cultured as previously described[73], and maintained in culture at 37°C, 5% CO_2 in MCDB/M199 medium supplemented with 10% FBS and penicillin/streptomycin.

Matched tumor specimens

Archival matched specimens of normal fallopian tube or ovary, ovarian tumor and omental tumor from high grade serous ovarian cancer patients were obtained through an honest broker from the ProMark biospecimens bank at the University of Pittsburgh Magee Womens Research Institute, with approval granted from the University of Pittsburgh IRB. Histological subtype and staging of tumor specimens shown in Extended Fig. 3b.

5'/3' Rapid amplification of cDNA ends (RACE)

3' and 5'RACE reactions were carried out using the SMARTer 3'5' RACE kit (Takara), essentially as recommended by the manufacturer. 5'RACE was carried out with the Universal Primer A Mix (UPM) and the *DNM1L* specific antisense primer, positioned in Exon 12: 5' GTTCCACACAGCGGAGGCTGGGC 3'. 3'RACE was carried out using *DNM1L* primer spanning the exon junction of exon 6/7: 5' GATTACGCCAAGCTTTGCCAGGAATGACCAAGGTGCCTGT-3', followed by nested PCR on the PCR product using *DNM1L* specific primers in exon 10/11: 5' GATTACGCCAAGCTTACTTCGGAGCTATGCGGTGGTGCT-3'. RACE PCR products were

resolved on a 10% agarose gel, bands gel purified and cloned into the pRACE vector for subsequent sequencing of inserts. Poly A sites were annotated to the *DNM1L* gene using the NCBI genome browser tracks for PolyA sites and clusters, Polyadenylation sits from PolyA_DB (v.3.2) and the polyadenylations sites from the PolyASites at the University of Basel.

Drp1/DNM1L variant RT-PCR

Total RNA from cells and tissue was isolated using Direct-zolTM RNA Miniprep kit (Zymo Research, R2052). Prior to RNA purification tissue was crushed under liquid Nitrogen and 25-50 mg of tissue-powder lysed in 800ml Ambion TRIzol Reagent (Invitrogen™,15596018) overnight at 4^{o}C. First-strand cDNA synthesis was performed using qScript cDNA Synthesis Kit (Quantabio, 95047) according to the manufacturer's instruction. RT-PCR was performed using diluted cDNA (1:5 in water) and PrimeStar DNA Polymerase (Takara, R010A) with primers and PCR conditions listed in Table 1. The amplified products, mixed with Gel Loading Buffer II (Thermo Scientific,AM8547), were separated on a PA-TBE gel and stained with GelStarTM Nucleic Acid Gel Stain (Lonza, 50535).

Primer	Sequence (S: sense; AS: antisense)	PCR Cycle
Drp1 Variable Domain Variants (Exons 16/17)	S: 5'-GGCAATTGAACTGGCTTATATCAACAC-3' AS: 5'-TGGTTGGTTCTTGAACACCATCTCCAA-3'	98C-15s, (98C-10s, 70C-15s, 72C-20s) X32
Drp1 ΔC truncated Variants	S: 5'-GGCAATTGAACTGGCTTATATCAACAC-3' AS: 5'-TAGATA CCACTACACAAACAGGTTCTT-3'	98C-15s, (98C-10s, 70C-15s, 72C-20s) X32-40
Total Drp1 (Exons 1-2)	S: 5'-GTGGGCCCCGGCCCCATTCAT-3' AS: 5'- CAGTACCTCTGGGAAGCAGGTCCCTCC-3'	95C-3m, (95C-10s, 68C-15s, 72C-20s) X32
Actin	S: 5'-AACTGGGACGACATGGAG-3' AS: 5'- TAGCACAGCCTGGATAGCAACGTA-3'	98C-15s, (98C-10s, 70C-15s, 72C-20s) X24

siRNA-mediated knock-down

Cells were transfected with scramble non-targeting SMARTpool control (Dharmacon#D-001810-10-05) or single or combination of Drp1 variant specific siRNA oligonucleotides against target sequence listed in Table 2 using Lipofectamine RNAiMAX (Invitrogen, 13778150). 48 hours post-transfection cells were seeded for experiments. For each experiment, knock-down was confirmed by RT-PCR using Drp1 variable domain variant RT-PCR primers, as above.

Drp1 siRNA	Target Sequence - 5'-3'	Target location

siDrp1(total)	GAGAAACAGGCTAGCCAGAGAATTACCTTCA	Exon 15
siDrp1(16/17)	GAGGCTGATGGCAAGTTAATTCAGGACAGCA	Exon 16/17 junction
siDrp1(-/17)	CTGTATCACGAGACAAGTTAATTCAGGACAG	Exon 15/17 junction
siDrp1(16/-)	GAGGCTGATGGCAAGGTTGCATCTGGAGGTG	Exon 16/18 junction
siDrp1(-/-)	CTGTATCACGAGACAAGGTTGCATCTGGAGG	Exon 15/18 junction

Immunoblotting

Cells were cultured to sub-confluency and lyzed in RIPA buffer (Thermo Scientific™, 89901) containing protease and phosphatase inhibitors (Thermo Scientific™, 78443). The protein supernatant was collected following 30 mins rotation at 4°C, followed by maximum speed (21,000 rcf) centrifugation for 30 mins in a 1.5 ml tabletop centrifuge at 4°C. Protein concentrations were measured using the Pierce BCA protein assay kit (Thermo Scientific™, 23225). Following SDS-PAGE, proteins were transferred to PVDF membranes. Membranes were blocked for an hour in in 5% non-fat milk (Bio-Rad,1706404)/TBS, 0.1% Tween20 (MilliporeSigma, 900-64-5) and were probed overnight at 4°C in primary antibodies. The next day blots were incubated for 1 hour at room temperature with horseradish peroxidase (HRP)-conjugated secondary antibodies and were developed using SuperSignal™ West Femto Maximum Sensitivity Substrate Femto (Thermo Scientific™, 34096).

Antibodies used:

Antibody	Manufacturer	Cat #	Dilution
Drp1	abcam	184247	1:1000
Drp1	EMD Millipore	ABT155	1:1000
Drp1/DLP1	BD Transduction	611112	1:1000
Phospho-DRP1 (Ser616)	Cell Signaling	3455	1:1000
MitoBiogenesis™ Western Blot Cocktail	abcam	123545	1:250
β-actin (9f3)	Thermo Scientific	AM4302	1:1000
β-tubulin (AC-15)	Cell Signaling	2128	1:1000
GAPDH (0411)	Santa Cruz	sc-47724	1:1000
Vinculin	Sigma-Aldrich	Aldrich V9131	1:1000
Amersham ECL HRP conjugated rabbit IgG	Cytiva	NA934	1:10000

Amersham ECL HRP conjugated mouse IgG	Cytiva	NA931	1:10000

TCGA data analysis

RNAseq bam files for the TCGA serous ovarian carcinoma cohort (n = 379, all cases regardless of grade and stage) were downloaded from dbGaP and stored on a secure server according to dbGaP protocols. The samtools 1.9.0 software [74] was used to convert each bam file to two fastq files corresponding to the paired end reads after randomizing the order of the reads with 'samtools collate.' The salmon 1.3.0 software [75] was then applied to quantify genome-wide transcript abundances based on an index created from a custom reference fasta file, as described below, that incorporates sequences from splice variants and alternate polyadenylation forms of DNML1. The --seqBias, --gcBias, and --validateMapping options for the salmon quant command were utilized. The salmon index was created by following the steps outlined at https://combine-lab.github.io/alevin-tutorial/2019/selective-alignment/. First, a decoys.txt file was created using the GRCh38 primary assembly fasta file. Next, a custom version of the gencode.v22.pc_transcripts.fa file was made by removing all transcripts corresponding to the DNML1 gene and replacing them with sequences corresponding to the alternative splice and alternative polyadenylated transcripts of *DNML1*. Concatenating this custom transcriptome fasta file with the GRCh38 primary assembly fasta file yielded the gentrome fasta file that, along with the decoys.txt file, was used to produce the salmon index. Overall survival data was obtained using cBioportal.

Drp1 plasmids & subcloning

Rat Drp1(-/17) and Drp1(16/17) cloned in pEGFP-C1 plasmids were kindly provided by Dr. Stefan Strack, University of Iowa [27]. Drp1 coding sequence were subcloned into pLenti-CMV-MCS-GFP-SV-puro (Addgene, 73582) with a N-terminal GFP tag and sequenced to confirm successful cloning of Drp1(-/17) and Drp1(16/17) plasmids. The plasmids were transfected in 293-FT cells for expression and lentiviral particle production. OVCA433 and SKOV3 cells were infected and transduced with the GFP vector control, GFP-Drp1(-/17) and GFP-Drp1(16/17) virus, selected for expression using 5ug/ml Puromycin for 1-2 weeks and sorted for GFP expression by flow cytometry to generate stable Drp1 overexpressing cells.

Immunofluorescence and analysis of mitochondrial morphology

Prior to imaging, mitochondria were labelled in cells by transduction with pLV-mitoDsRed virus (Addgene, Plasmid 44386) harvested post expression in 293-FT cells and lentiviral particle production. For imaging, cells were seeded at 60-70% confluency in Chambered Cell Culture slides (Falcon, 08-774-25). Next day, cells were washed once with 1X PBS (Corning, 21-040-CV) and fixed in 4% formaldehyde, made fresh by diluting 16% PFA solution (BTC BeanTown Chemical,30525-89-4) in 1X PBS for 10 mins at room temperature. For imaging FCCP treatment, cells were incubated with 1μM FCCP(Sigma) in media for 30 mins prior to fixation. Post fixation, cells were rinsed twice with 1X PBS and permeabilized for 10-15 mins using 0.2 % Triton™ X-100 (Fisher Scientific, BP151500) in 1X PBS with gentle rocking. Followed by two more PBS rinses prior to 1 hour incubation with SuperBlock™ Blocking Buffer (Thermo Scientific™,37515) for blocking non-specific antibody binding. Cells were stained with primary antibody against Tubulin (Abcam, ab6160) at 1:1000 dilution in SuperBlock™ blocking buffer for either 1hr 30 mins at room temperature or overnight at 4°C. After incubation cells were washed for three subsequent 10 min washes with 1X PBS with gently rocking. Cells were incubated with 1:1000 dilution of secondary rat antibody conjugated with Alexa Fluor® 647 (abcam, 150167) in SuperBlock™ Blocking Buffer at room temperature for 30 mins. After, washed with 1X PBS for three times,10 mins each to remove any residual antibody. Slides were mounted in ProLong™ Gold Antifade Mountant with DNA Stain DAPI (Invitrogen™, P36935) and dried overnight in dark at room temperature. For mitochondrial imaging of SKOV3 post siRNA transfection, cells were seeded on 35mm glass bottom dishes (MatTek, P35GC-1.5-14-C). Next day cells were stained using MitoTracker™ Green FM (Invitrogen™, M7514) following the manufacturer's recommendations. Briefly, cells were incubated for 12-15 mins in pre-warmed culture medium containing 250 nM MitoTracker™ Green FM and Hoechst 33342 (Thermo Scientific™,62249). After, cells were washed thrice with 1X PBS and imaged in pre-warmed 1X HBSS (Corning, 21-023-CV). Z-stacks were taken with Leica Thunder Imager using 63X oil immersion objective and subjected to inbuilt thunder de-convolution. The mitochondrial network morphology to look at the elongation and fragmentation was performed on 2D Z-stack projections in image J using the mitochondria-analyzer plugin (https://github.com/AhsenChaudhry/Mitochondria-Analyzer). Briefly, the images were converted into binary, and threshold was adjusted to detect the mitochondrial network before performing the 2D per-cell mitochondrial network analysis. Total of at least 150 or more cells were analyzed to get the morphological network parameters with 30 cells or more. analyzed for each biological replicate over at least 3 or more biological replicates. Representative images shown were adjusted in brightness and contrast for better visualization.

TEM

Cells were fixed in cold 2.5% glutaraldehyde (25% glutaraldehyde stock EM grade, Polysciences, 111-30-8) in 0.01 M PBS (Fisher), pH 7.3. Samples were rinsed in PBS, post-fixed in 1% osmium tetroxide (Electron Microscopy Sciences) with 1% potassium ferricyanide, (Fisher), rinsed in PBS, dehydrated through a graded series of ethanol, and embedded in Poly/Bed® 812 (Luft formulations). Semi-thin (300 nm) sections were cut on a Reichart Ultracut (Leica Microsystems), stained with 0.5% Toluidine Blue O (Fisher) in 1% sodium borate (Fisher) and examined under the light microscope. Ultrathin sections (65 nm) were stained with 2% uranyl acetate (Electron Microscopy Science) and Reynold's lead citrate (Lead Nitrate, Sodium Citrate and Sodium Hydroxide, Fisher) and examined on JEOL 1400 Plus transmission electron microscope with a side mount AMT 2k digital camera (Advanced Microscopy Techniques). For morphometric analysis of mitochondria by transmission electron microscopy, mitochondrial area, mitochondrial length (major axis), cristae number and cristae volume density per mitochondria was quantified and analyzed as described[76] using ImageJ. At least 40-50 mitochondria per biological replicate over 3 experimental replicates were analyzed.

TMRE Protocol

OVCA433 and SKOV3 were seeded into 96-well plates at a density of 1,000 cells per well and incubated overnight in a cell culture incubator at 37ºC and 5% CO_2. The following day, half the sample wells were treated with 10 µM FCCP and incubated for 30 minutes in a cell culture incubator. All the sample wells were then treated with 100 nM TMRE (Thermo Fisher Scientific, T669), and incubated for 30 minutes at 37ºC in a cell culture incubator. All samples were subsequently washed twice with 1X PBS, and fluorescence measurements were taken with a Synergy HT microplate reader (BioTek) with an excitation wavelength of 530 nm and emission wavelength of 590 nm.

MitoSox mitochondrial superoxide indicator

500,000 cells were stained with 5 µM MitoSOX Red mitochondrial superoxide indicator (Invitrogen, M36008) in 1 ml HBSS (Corning, 21-023-CV) for 30 minutes at 37ºC. Following incubation, cells were washed with HBSS, and florescence was measured using flow cytometry as per manufacture's protocol. Unstained cells were used as a negative control while cells treated with 50 µM Antimycin A were used as a positive control for flow cytometry.

Bioenergetic Analysis of Oxygen Consumption Rate (OCR) and Extracellular Acidification Rate (ECAR)

The Agilent Seahorse XFp Metabolic Analyzer (Agilent, model S7802A) was used to assess mitochondrial respiration of OVCA433 and SKOV3 as described previously for attached cells[77]. Briefly, prior to the start of the experiment, cells were evenly seeded and cultured overnight in a Seahorse XFp cell culture plate (Agilent, 103022-100) at a density of 10,000 and 8,000 cells/well for OVCA433 and SKOV3, respectively. The XFp sensor cartridge was hydrated in Agilent Seahorse XF Calibrant (Agilent,103022-100) at 37°C in a humidified incubator (non-CO_2) incubator overnight. On the day of the experiment, cell culture media was replaced with pre-warmed seahorse XF base RPMI media, pH 7.4 (Agilent,103576-100) supplemented with 1 mM sodium pyruvate (Agilent 103578-100), 2 mM glutamine (Agilent 103579-100), and 10 mM glucose (Agilent, 103577-100). Cells were then placed into a non-CO_2 humidified incubator at 37°C for 60 min. Mitochondrial stress test reagents (pharmacological manipulators of mitochondrial respiratory chain proteins) were diluted in pre-warmed XF assay media to achieve the following final concentrations in the cell culture well: 1.5 μM Oligomycin A (Sigma, 75351); 1 or 0.5 μM FCCP (Sigma, C2920) for OVCA433 and SKOV3, respectively; and 0.5 μM Antimycin A/Rotenone (Sigma, A8674,45656). Three basal rate measurements (3 min measurement time each) were taken prior to the injection of mitochondrial stress test reagents and three measurements of OCR/ECAR were obtained respectively following injection of compounds. Post-run, the cells were stained with crystal violet dye (0.05%) (Sigma-Aldrich, 229288) for seeding normalization. The dye was released from cells using 30% acetic acid and absorbance was measured at 590 nm, using GloMax Explorer (Promega) microplate reader.

Metabolomics

1-2 million cells were seeded in 60 mm dishes per replicate (n=6 for each condition) in normal cell growth media. Next day, cells were washed once with 1X PBS and fresh media was added. After 24 hours, metabolic quenching and polar metabolite pool extraction was performed by adding ice cold 80% methanol (aqueous with 0.1% formic acid) at a ratio of 500µL buffer per 1e6 cells. Deuterated (D3)-creatinine and (D3)-alanine, (D4)-taurine and (D3)-lactate (Sigma-Aldrich) was added to the sample lysates as an internal standard for a final concentration of 10µM. Samples are scraped into Eppendorf tubes on ice, homogenized using a 25°C water bath sonicator and the supernatant was then cleared of protein by centrifugation at 16,000xg. 2µL of cleared supernatant was subjected to online LC-MS analysis. Analyses were performed by untargeted LC-HRMS. Briefly, Samples were injected via a Thermo Vanquish UHPLC and separated over a reversed phase Thermo HyperCarb porous graphite column (2.1×100mm, 3µm particle size) maintained at 55°C. For the 20 minute LC gradient, the mobile phase

consisted of the following: solvent A (water / 0.1% FA) and solvent B (ACN / 0.1% FA). The gradient was the following: 0-1min 1% B, increase to 15%B over 5 minutes, continue increasing to 98%B over 5 minutes, hold at 98%B for five minutes, reequillibrate at 1%B for five minutes. The Thermo IDX tribrid mass spectrometer was operated in both positive and ion mode, scanning in ddMS2 mode (2 μscans) from 70 to 800 m/z at 120,000 resolution with an AGC target of 2e5 for full scan, 2e4 for ms2 scans using HCD fragmentation at stepped 15,35,50 collision energies. Source ionization setting was 3.0 and 2.4kV spray voltage respectively for positive and negative mode. Source gas parameters were 35 sheath gas, 12 auxiliary gas at 320°C, and 8 sweep gas. Calibration was performed prior to analysis using the PierceTM FlexMix Ion Calibration Solutions (Thermo Fisher Scientific). Integrated peak areas were then extracted manually using Quan Browser (Thermo Fisher Xcalibur ver. 2.7).

NAD^+ and NADH level determination

OVCA433 and SKOV3 cells were seeded into flat-bottom 96-well plates at a density of 10,000 and 8,000 respectively in normal growth medium. After overnight incubation, total NAD+ and NADH levels and their ratios were determined using NAD+/NADH-glo assay kit (Promega, G9071) as per manufacture's protocol. Following addition of NAD/NADH-GloTM Detection Reagent, samples were incubated for 1 hour at room temperature and transferred to white flat-bottom 96-well plate (BrandTech® ,BRA-781605). Bioluminescence was measured with GloMax Explorer (Promega) plate reader. Protein Concertation was determined by BCA and used for data normalization.

Cell proliferation and viability

Equal number of cells were seeded into 96 well plates at density of 1000 and 500 cells/well for OVCA433 and SKOV3 respectively, in normal culture medium. For cell proliferation rate, cell numbers were analyzed for 3 days successively using FluoReporter™ Blue Fluorometric dsDNA Quantitation Kit (Invitrogen™, F2962) as per manufacturer's protocol and fluorescence measurements were taken with a Victor X (PerkinElmer) microplate reader with an excitation wavelength of 360 nm and emission wavelength of 460 nm respectively. Proliferation rate was measured as the increase in the cell density relative to day 1. For cell viability in response to chemotherapeutic agents, cells were treated with indicated doses of Cisplatin (cis-Diamineplatinum(II) dichloride) (Sigma) or Paclitaxel(Sigma). Following 72 hours of drug treatment cell viability was measured using FluoReporter™ Blue Fluorometric dsDNA Quantitation Kit and was expressed as percentage survival relative to non-treated cells.

Caspase 3/7 activity assay

OVCA433 and SKOV3 cells were seeded into flat-bottom 96-well plates at a density of 7,000 and 5,000 cells per well respectively in normal growth medium. After overnight incubation, cells were treated with 5 μM Cisplatin (cis-Diamineplatinum(II) dichloride) (Sigma) or 1 nM Paclitaxel (Sigma) respectively. After 24 hours drug treatment, caspase 3/7 activity was measured using Caspase-Glo® 3/7 Assay System- (Promega, G8091) per manufacture's protocol. Briefly, equal volume of reagent was added to the samples and only media control. Following 1 hour incubation in dark at room temperature, samples were transferred to white flat-bottom 96-well plate (BrandTech®, BRA-781605) and bioluminescence was measured with GloMax Explorer (Promega) plate reader.

Clonogenicity assay

100 cells/well were seeded in a 6 well plate for single cell survival clonogenicity assay and cultured for 7-10 days under normal culture conditions. Clonogenicity was assessed by staining colonies with crystal violet (0.05%). Colonies were counted using Image J and data expressed as cellular survival fraction.

Migration Assay

For assessment of Transwell migration, cell culture inserts (Corning, 353097) with 8.0 μm Transparent PET Membrane, were each placed into a 24- well plate with 800 μL complete growth medium (with serum) added at the bottom of each well. 50,000 and 30,000 cells of OVCA433 and SKOV3, respectively were seeded onto the top of the Transwell membrane of the insert in 150 μL serum free media. After 24 hours, the Transwelll inserts were removed and washed twice with 1XPBS. The Transwell membrane was fixed and stained with Crystal violet (0.05%) for an hour. The inserts were washed three times with 1X PBS and the non-migrated cells were removed from the top of the membrane using dry cotton swabs. The inserts were dried overnight, and images were taken of the migrated cells at the bottom of the membrane using Leica Thunder Imager with colored K3C camera. The dye was released from cell inserts using 30% acetic acid and absorbance was measured using GloMax Explorer (Promega) microplate reader at 590 nm as a readout for cell migration.

Tumor xenografts

Approval for animal studies was sought from the University of Pittsburgh IACUC prior to study commencement. All the animal experiments were performed in accordance with the guidelines

of the Laboratory Animal Ethics Committee of Pittsburgh University, and mice randomized prior to tumor cell injection and drug treatment. For Intraperitoneal xenografts 2× 10^6 SKOV3 cells expressing either GFP control, GFP-Drp1(-/17) and GFP-Drp1(16/17) were suspended in 0.2ml PBS and injected IP into female Nod *scid* gamma mice (NSG, Jackson laboratory; n=10). Luminescence imaging was carried out on days indicated using an IVIS luminescence imaging system 10 min after mice were injected with 10 µl/g of body weight 15 mg/mL *in vivo* grade D-Luciferin (PerkinElmer, 122799). Mice were sacrificed when reaching AAALAC-defined endpoints by CO_2 asphyxiation followed by cervical dislocation. At necropsy organs and tumor mass were weighed, and tissues fixed in 10% buffered formalin (Fisher Scientific, 5735), followed by paraffin embedding, sectioning, and H&E staining. For Subcutaneous (SC) tumor xenografts SKOV3 cells expressing GFP, Drp1(-/17) and Drp1(16/17) were counted (5× 10^6) and prepared as suspensions in 0.2ml PBS for both right and left subcutaneous (flank) injections into 6–8 week old CrTac:NCr-*Foxn1*^{nu} female mice (Taconic) in groups of 4-5 mice with total 8-10 tumor site injections per group. Mice were injected IP with Cisplatin (5 mg/kg body weight) or vehicle control (PBS) on days 7, 11, 15, 22, 29, 32, 36, and 40 post tumor cell injection. Subcutaneous tumor growth was monitored using caliper measurements twice weekly and tumor volumes calculated according to the formula V= ½ (length (longer diameter) × width (shorter diameter)^2). All vehicle treated groups were euthanized on the same day (Day 49) to compare basal tumor growth rates. Cisplatin treated mice continued to be monitored for chemotherapy response and progression free survival determined by tumor sizes of less than 200m^3. Mice were euthanized by CO_2 asphyxiation followed by cervical dislocation when tumors reached >1500mm^3 or other AAALAC endpoints were met. At endpoint, the xenografted tumors were resected and weighed.

Data and Statistical Analysis

All data presented are from at least three biological replicates and represented as mean ± standard error of the mean. Unless otherwise indicated, statistical data analysis was carried out using GraphPad Prism Software (10.0.2), with appropriate analyses chosen based on experimental design, as stated in figure legends.

Acknowledgements

The authors would like to thank Dr. Stefan Strack for providing Drp1 splice variant plasmids. We would like to thank Yisang Yoon, Janine Santos, and Patrick Kimes for helpful scientific discussions. We thank Royden Clark, Emmy Dier, Sara Shimko and Ben Yankasky for technical

assistance. This work was supported by the U.S. Department of Defense CDMRP pilot award W81XWH-16-1-0117, TEAL award W81XWH-22-10252 and NIH R01CA242021 (to N.H.), R01CA230628 (to K.M. & N.H), NIH training grant 2T32HL110849-11A1 (to S.W.), R35-HL150778 (to M.T.), NIHS10OD023402 (to S.L.G.) and NIH instrumentation grants S10RR025488, S10RR016236, S10RR019003 (to S.C.W.). Lauren Borho and Dr. Francesmary Mudugno kindly assisted as honest brokers to access patient specimens. The ProMark tissue bank is supported by NIH SPORE P50CA272218. This project used the Hillman Cancer Center Cytometry Facility, Animal Facility, In vivo Imaging Facility and Cell and Tissue Imaging Facility that are supported in part by award P30CA047904.

Author contributions

Z.J. contributed to conceptual and experimental design, carried out experiments and data analysis, prepared figures and wrote the manuscript. D.H.S contributed to experimental design, carried out experiments and data analysis. W.P., S.W., A.E., S.K., Y.-Y.C., J.C.B., A.E.A., M.S., S.J.M., carried out experiments and performed data analysis. S.C.W., C.M.S.C, S.G.W., assisted with experimental design and technical guidance. R.P., H.G.W., S.Y., N.L., L.G.C., K.M.A. contributed to conceptual ideas and manuscript editing. M.T., V.W., and K.M. contributed to conceptual and experimental design, data analysis and interpretation, and manuscript editing. N.H. supervised and conceived the study, contributed to conceptual and experimental design, assisted in data analysis, writing and editing of the manuscript.

Ethics declarations

The authors declare no competing interests.

Data availability

Source data are provided with the manuscript and can be obtained upon reasonable request from the corresponding author.

References

1. Kamerkar, S.C., Kraus, F., Sharpe, A.J., Pucadyil, T.J. & Ryan, M.T. Dynamin-related protein 1 has membrane constricting and severing abilities sufficient for mitochondrial and peroxisomal fission. *Nat Commun* **9**, 5239 (2018).
2. Archer, S.L. Mitochondrial dynamics--mitochondrial fission and fusion in human diseases. *N Engl J Med* **369**, 2236-2251 (2013).

3. Santel, A. & Frank, S. Shaping mitochondria: The complex posttranslational regulation of the mitochondrial fission protein DRP1. *IUBMB Life* **60**, 448-455 (2008).
4. Yu, R. *et al.* The Molecular Assembly State of Drp1 Controls its Association With the Mitochondrial Recruitment Receptors Mff and MIEF1/2. *Front Cell Dev Biol* **9**, 706687 (2021).
5. Yamada, T., Adachi, Y., Iijima, M. & Sesaki, H. Making a Division Apparatus on Mitochondria. *Trends Biochem Sci* **41**, 209-210 (2016).
6. Cribbs, J.T. & Strack, S. Reversible phosphorylation of Drp1 by cyclic AMP-dependent protein kinase and calcineurin regulates mitochondrial fission and cell death. *EMBO Rep* **8**, 939-944 (2007).
7. Strack, S. & Cribbs, J.T. Allosteric modulation of Drp1 mechanoenzyme assembly and mitochondrial fission by the variable domain. *J Biol Chem* **287**, 10990-11001 (2012).
8. Parone, P.A. *et al.* Preventing mitochondrial fission impairs mitochondrial function and leads to loss of mitochondrial DNA. *PLoS One* **3**, e3257 (2008).
9. Benard, G. *et al.* Mitochondrial bioenergetics and structural network organization. *J Cell Sci* **120**, 838-848 (2007).
10. Twig, G. *et al.* Fission and selective fusion govern mitochondrial segregation and elimination by autophagy. *EMBO J* **27**, 433-446 (2008).
11. Arnoult, D. *et al.* Bax/Bak-dependent release of DDP/TIMM8a promotes Drp1-mediated mitochondrial fission and mitoptosis during programmed cell death. *Curr Biol* **15**, 2112-2118 (2005).
12. Tanwar, D.K. *et al.* Crosstalk between the mitochondrial fission protein, Drp1, and the cell cycle is identified across various cancer types and can impact survival of epithelial ovarian cancer patients. *Oncotarget* **7**, 60021-60037 (2016).
13. Serasinghe, M.N. *et al.* Mitochondrial division is requisite to RAS-induced transformation and targeted by oncogenic MAPK pathway inhibitors. *Mol Cell* **57**, 521-536 (2015).
14. Kashatus, J.A. *et al.* Erk2 phosphorylation of Drp1 promotes mitochondrial fission and MAPK-driven tumor growth. *Mol Cell* **57**, 537-551 (2015).
15. Taguchi, N., Ishihara, N., Jofuku, A., Oka, T. & Mihara, K. Mitotic phosphorylation of dynamin-related GTPase Drp1 participates in mitochondrial fission. *J Biol Chem* **282**, 11521-11529 (2007).
16. Rehman, J. *et al.* Inhibition of mitochondrial fission prevents cell cycle progression in lung cancer. *FASEB journal : official publication of the Federation of American Societies for Experimental Biology* **26**, 2175-2186 (2012).

17. Desai, S.P., Bhatia, S.N., Toner, M. & Irimia, D. Mitochondrial localization and the persistent migration of epithelial cancer cells. *Biophys J* **104**, 2077-2088 (2013).
18. Wieder, S.Y. *et al.* Activation of the Mitochondrial Fragmentation Protein DRP1 Correlates with BRAF(V600E) Melanoma. *J Invest Dermatol* **135**, 2544-2547 (2015).
19. Frank, S. *et al.* The role of dynamin-related protein 1, a mediator of mitochondrial fission, in apoptosis. *Developmental cell* **1**, 515-525 (2001).
20. Thomas, K.J. & Jacobson, M.R. Defects in mitochondrial fission protein dynamin-related protein 1 are linked to apoptotic resistance and autophagy in a lung cancer model. *PLoS One* **7**, e45319 (2012).
21. Caino, M.C. *et al.* PI3K therapy reprograms mitochondrial trafficking to fuel tumor cell invasion. *Proc Natl Acad Sci U S A* **112**, 8638-8643 (2015).
22. Farrand, L. *et al.* An improved quantitative approach for the assessment of mitochondrial fragmentation in chemoresistant ovarian cancer cells. *PLoS One* **8**, e74008 (2013).
23. Kong, B., Wang, Q., Fung, E., Xue, K. & Tsang, B.K. p53 is required for cisplatin-induced processing of the mitochondrial fusion protein L-Opa1 that is mediated by the mitochondrial metallopeptidase Oma1 in gynecologic cancers. *J Biol Chem* **289**, 27134-27145 (2014).
24. Macdonald, P.J. *et al.* Distinct Splice Variants of Dynamin-related Protein 1 Differentially Utilize Mitochondrial Fission Factor as an Effector of Cooperative GTPase Activity. *J Biol Chem* **291**, 493-507 (2016).
25. Rosdah, A.A. *et al.* New perspectives on the role of Drp1 isoforms in regulating mitochondrial pathophysiology. *Pharmacol Ther* **213**, 107594 (2020).
26. Itoh, K. *et al.* A brain-enriched Drp1 isoform associates with lysosomes, late endosomes, and the plasma membrane. *J Biol Chem* **293**, 11809-11822 (2018).
27. Strack, S., Wilson, T.J. & Cribbs, J.T. Cyclin-dependent kinases regulate splice-specific targeting of dynamin-related protein 1 to microtubules. *J Cell Biol* **201**, 1037-1051 (2013).
28. Howng, S.L. *et al.* Genomic organization, alternative splicing, and promoter analysis of human dynamin-like protein gene. *Biochem Biophys Res Commun* **314**, 766-772 (2004).
29. Chen, C.H. *et al.* Differential expression of four human dynamin-like protein variants in brain tumors. *DNA Cell Biol* **19**, 189-194 (2000).
30. Tsuyoshi, H. *et al.* Prognostic impact of Dynamin related protein 1 (Drp1) in epithelial ovarian cancer. *BMC Cancer* **20**, 467 (2020).

31. Dier, U., Shin, D.H., Hemachandra, L.P., Uusitalo, L.M. & Hempel, N. Bioenergetic analysis of ovarian cancer cell lines: profiling of histological subtypes and identification of a mitochondria-defective cell line. *PLoS One* **9**, e98479 (2014).
32. Uo, T. *et al.* Drp1 levels constitutively regulate mitochondrial dynamics and cell survival in cortical neurons. *Exp Neurol* **218**, 274-285 (2009).
33. Yoon, Y., Pitts, K.R., Dahan, S. & McNiven, M.A. A novel dynamin-like protein associates with cytoplasmic vesicles and tubules of the endoplasmic reticulum in mammalian cells. *J Cell Biol* **140**, 779-793 (1998).
34. Michalska, B.M. *et al.* Insight into the fission mechanism by quantitative characterization of Drp1 protein distribution in the living cell. *Sci Rep* **8**, 8122 (2018).
35. Li, J. *et al.* Mitochondrial elongation-mediated glucose metabolism reprogramming is essential for tumour cell survival during energy stress. *Oncogene* **36**, 4901-4912 (2017).
36. Skulachev, V.P. Mitochondrial filaments and clusters as intracellular power-transmitting cables. *Trends Biochem Sci* **26**, 23-29 (2001).
37. Varanita, T. *et al.* The OPA1-dependent mitochondrial cristae remodeling pathway controls atrophic, apoptotic, and ischemic tissue damage. *Cell Metab* **21**, 834-844 (2015).
38. Cogliati, S. *et al.* Mitochondrial cristae shape determines respiratory chain supercomplexes assembly and respiratory efficiency. *Cell* **155**, 160-171 (2013).
39. Cogliati, S., Enriquez, J.A. & Scorrano, L. Mitochondrial Cristae: Where Beauty Meets Functionality. *Trends Biochem Sci* **41**, 261-273 (2016).
40. Karbowski, M. *et al.* Spatial and temporal association of Bax with mitochondrial fission sites, Drp1, and Mfn2 during apoptosis. *J Cell Biol* **159**, 931-938 (2002).
41. Fonseca, T.B., Sanchez-Guerrero, A., Milosevic, I. & Raimundo, N. Mitochondrial fission requires DRP1 but not dynamins. *Nature* **570**, E34-E42 (2019).
42. Otera, H. *et al.* Mff is an essential factor for mitochondrial recruitment of Drp1 during mitochondrial fission in mammalian cells. *J Cell Biol* **191**, 1141-1158 (2010).
43. Mopert, K. *et al.* Loss of Drp1 function alters OPA1 processing and changes mitochondrial membrane organization. *Exp Cell Res* **315**, 2165-2180 (2009).
44. Lima, A.R. *et al.* Dynamin-Related Protein 1 at the Crossroads of Cancer. *Genes (Basel)* **9** (2018).
45. Banerjee, R., Mukherjee, A. & Nagotu, S. Mitochondrial dynamics and its impact on human health and diseases: inside the DRP1 blackbox. *J Mol Med (Berl)* **100**, 1-21 (2022).

46. Xie, Q. *et al.* Mitochondrial control by DRP1 in brain tumor initiating cells. *Nat Neurosci* **18**, 501-510 (2015).
47. Ciesla, M. *et al.* Oncogenic translation directs spliceosome dynamics revealing an integral role for SF3A3 in breast cancer. *Mol Cell* **81**, 1453-1468 e1412 (2021).
48. Gao, T. *et al.* SIK2 promotes reprogramming of glucose metabolism through PI3K/AKT/HIF-1alpha pathway and Drp1-mediated mitochondrial fission in ovarian cancer. *Cancer Lett* **469**, 89-101 (2020).
49. van der Bliek, A.M. Fussy mitochondria fuse in response to stress. *EMBO J* **28**, 1533-1534 (2009).
50. Tondera, D. *et al.* SLP-2 is required for stress-induced mitochondrial hyperfusion. *EMBO J* **28**, 1589-1600 (2009).
51. Grieco, J.P. *et al.* Progression-Mediated Changes in Mitochondrial Morphology Promotes Adaptation to Hypoxic Peritoneal Conditions in Serous Ovarian Cancer. *Front Oncol* **10**, 600113 (2020).
52. Anderson, A.S., Roberts, P.C., Frisard, M.I., Hulver, M.W. & Schmelz, E.M. Ovarian tumor-initiating cells display a flexible metabolism. *Exp Cell Res* **328**, 44-57 (2014).
53. Ngo, J. *et al.* Mitochondrial morphology controls fatty acid utilization by changing CPT1 sensitivity to malonyl-CoA. *EMBO J* **42**, e111901 (2023).
54. Alan, L. & Scorrano, L. Shaping fuel utilization by mitochondria. *Curr Biol* **32**, R618-R623 (2022).
55. Liesa, M. & Shirihai, O.S. Mitochondrial dynamics in the regulation of nutrient utilization and energy expenditure. *Cell Metab* **17**, 491-506 (2013).
56. Dar, S. *et al.* Bioenergetic Adaptations in Chemoresistant Ovarian Cancer Cells. *Sci Rep* **7**, 8760 (2017).
57. Bellance, N. *et al.* Bioenergetics of lung tumors: alteration of mitochondrial biogenesis and respiratory capacity. *Int J Biochem Cell Biol* **41**, 2566-2577 (2009).
58. Ghoneum, A., Gonzalez, D., Abdulfattah, A.Y. & Said, N. Metabolic Plasticity in Ovarian Cancer Stem Cells. *Cancers (Basel)* **12** (2020).
59. Yang, L. *et al.* Metabolic shifts toward glutamine regulate tumor growth, invasion and bioenergetics in ovarian cancer. *Mol Syst Biol* **10**, 728 (2014).
60. Pasto, A. *et al.* Cancer stem cells from epithelial ovarian cancer patients privilege oxidative phosphorylation, and resist glucose deprivation. *Oncotarget* **5**, 4305-4319 (2014).

61. Denkert, C. *et al.* Mass spectrometry-based metabolic profiling reveals different metabolite patterns in invasive ovarian carcinomas and ovarian borderline tumors. *Cancer Res* **66**, 10795-10804 (2006).
62. Fong, M.Y., McDunn, J. & Kakar, S.S. Identification of metabolites in the normal ovary and their transformation in primary and metastatic ovarian cancer. *PLoS One* **6**, e19963 (2011).
63. Mitra, K., Wunder, C., Roysam, B., Lin, G. & Lippincott-Schwartz, J. A hyperfused mitochondrial state achieved at G1-S regulates cyclin E buildup and entry into S phase. *Proc Natl Acad Sci U S A* **106**, 11960-11965 (2009).
64. Spurlock, B. *et al.* Fine-tuned repression of Drp1-driven mitochondrial fission primes a 'stem/progenitor-like state' to support neoplastic transformation. *Elife* **10** (2021).
65. Zampieri, L.X. *et al.* Mitochondria Participate in Chemoresistance to Cisplatin in Human Ovarian Cancer Cells. *Mol Cancer Res* **18**, 1379-1391 (2020).
66. Farge, T. *et al.* Chemotherapy-Resistant Human Acute Myeloid Leukemia Cells Are Not Enriched for Leukemic Stem Cells but Require Oxidative Metabolism. *Cancer Discov* **7**, 716-735 (2017).
67. Kong, B., Wang, Q., Fung, E., Xue, K. & Tsang, B.K. p53 is required for cisplatin-induced processing of the mitochondrial fusion protein L-Opa1 that is mediated by the mitochondrial metallopeptidase Oma1 in gynecologic cancers. *J Biol Chem* **289**, 27134-27145 (2014).
68. Zou, G.P. *et al.* Mitochondrial Dynamics Mediated by DRP1 and MFN2 Contributes to Cisplatin Chemoresistance in Human Ovarian Cancer SKOV3 cells. *J Cancer* **12**, 7358-7373 (2021).
69. Tien, J.F. *et al.* CDK12 regulates alternative last exon mRNA splicing and promotes breast cancer cell invasion. *Nucleic Acids Res* **45**, 6698-6716 (2017).
70. Song, X. *et al.* SRSF3-Regulated RNA Alternative Splicing Promotes Glioblastoma Tumorigenicity by Affecting Multiple Cellular Processes. *Cancer Res* **79**, 5288-5301 (2019).
71. Zhu, J., Chen, Z. & Yong, L. Systematic profiling of alternative splicing signature reveals prognostic predictor for ovarian cancer. *Gynecol Oncol* **148**, 368-374 (2018).
72. He, X. *et al.* Knockdown of splicing factor SRp20 causes apoptosis in ovarian cancer cells and its expression is associated with malignancy of epithelial ovarian cancer. *Oncogene* **30**, 356-365 (2011).

73. Shepherd, T.G., Theriault, B.L., Campbell, E.J. & Nachtigal, M.W. Primary culture of ovarian surface epithelial cells and ascites-derived ovarian cancer cells from patients. *Nat Protoc* **1**, 2643-2649 (2006).
74. Li, H. *et al.* The Sequence Alignment/Map format and SAMtools. *Bioinformatics* **25**, 2078-2079 (2009).
75. Patro, R., Duggal, G., Love, M.I., Irizarry, R.A. & Kingsford, C. Salmon provides fast and bias-aware quantification of transcript expression. *Nat Methods* **14**, 417-419 (2017).
76. Lam, J. *et al.* A Universal Approach to Analyzing Transmission Electron Microscopy with ImageJ. *Cells* **10** (2021).
77. Javed, Z. *et al.* Optimization of Extracellular Flux Assay to Measure Respiration of Anchorage-independent Tumor Cell Spheroids. *Bio Protoc* **12**, e4321 (2022).

Figures

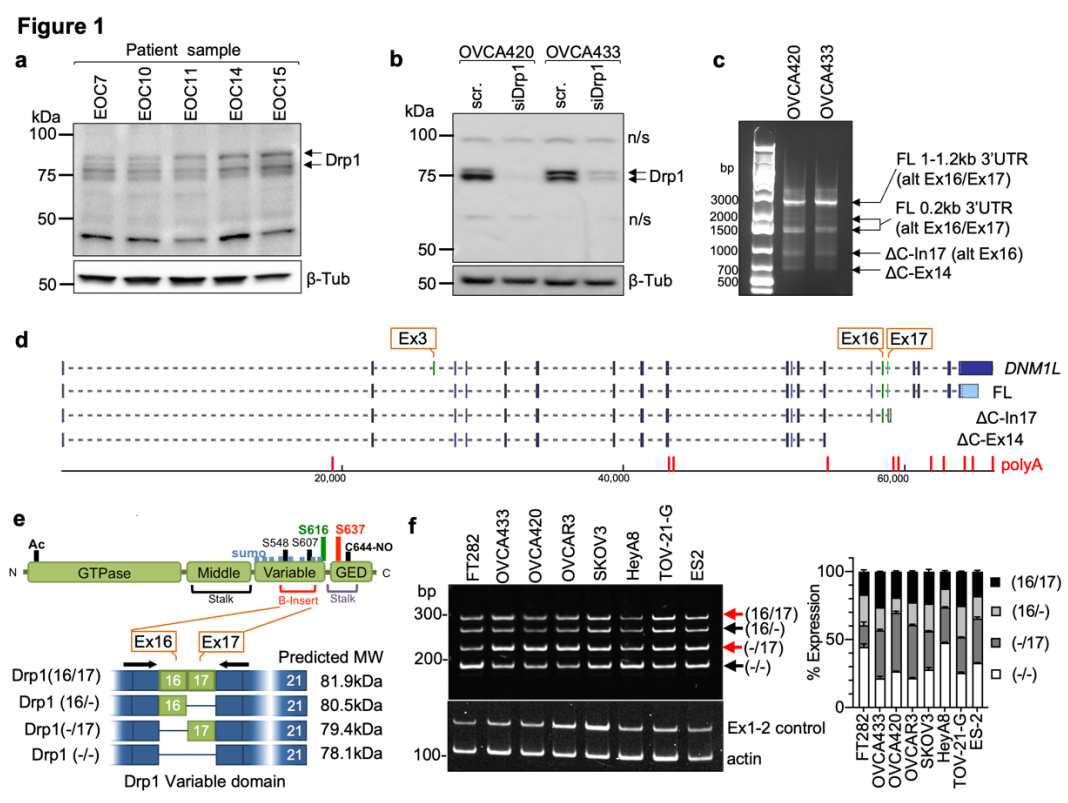

Figure 1. Ovarian cancer cells express splice variants of Drp1/*DNM1L*.

a. Western blot analysis of Drp1 protein expression in patient ascites derived epithelial ovarian cancer cells (EOC), with the following histological classification: EOC7: HGSA stage IC; EOC10: granulosa tumor IV; EOC 11: carcinosarcoma stage IIIB; EOC14: HGSA stage IV; EOC15: HGSA stage IV. Arrows point to the predicted molecular weight protein (upper arrow) and a lower molecular weight band, that is prominently expressed in EOCs from patient ascites.

b. Drp1 protein variants identified in OVCA420 and OVCA433 cells by western blotting using the N-terminal anti-Drp1 monoclonal antibody ab184247. Specificity to Drp1 was assessed by siRNA mediated knock-down. Potential non-specific bands (n/s) are indicated. One representative blot from 3 independent replicates shown.

c. 3' RACE and subsequent sequencing of PCR products reveals that OVCA420 and OVCA433 cells express multiple *DNM1L* transcripts variants, including full length (FL) transcripts with alternatively spliced exons 16 and 17, and C terminal truncated transcripts at exon 14 (ΔC-Ex14) and intron 17 (ΔC-In17).

d. Schematic of transcript variants identified in OVCA420 and OVCA433 cells by 5' and 3' RACE (from panel c), including alternative splicing of the variable domain exons 16 and 17 (panel c: alt Ex 16/17); variable lengths of 3'UTRs (panel c: FL 1-1.2kb, 0.2kb 3'UTR), and utilization of alternate proximal polyadenylation, resulting in two C terminal truncation variants, terminating in Intron 17 (ΔC-In17) and exon 14 (ΔC-Ex14). ΔC-In17 has two variants due to exon 16 alternative splicing and has a predicted STOP codon following a novel coding sequence for 16 amino acids within intron 17.

e. Schematic representation of the Drp1/*DNM1L* protein sequence functional domains and areas of post-translational modifications. The location of alternative spliced exons 16 and 17 is in the variable B-insert domain. Numbers in brackets of transcript names denote included exons in of the variable domain, dash denotes exon is spliced out.
f. RT-PCR with primers flanking the variable domain illustrates relative expression of the four *DNM1L* variable domain splice variants derived from alternative splicing of exons 16 and 17 in ovarian cancer cell lines (n=3, mean +/- SEM).

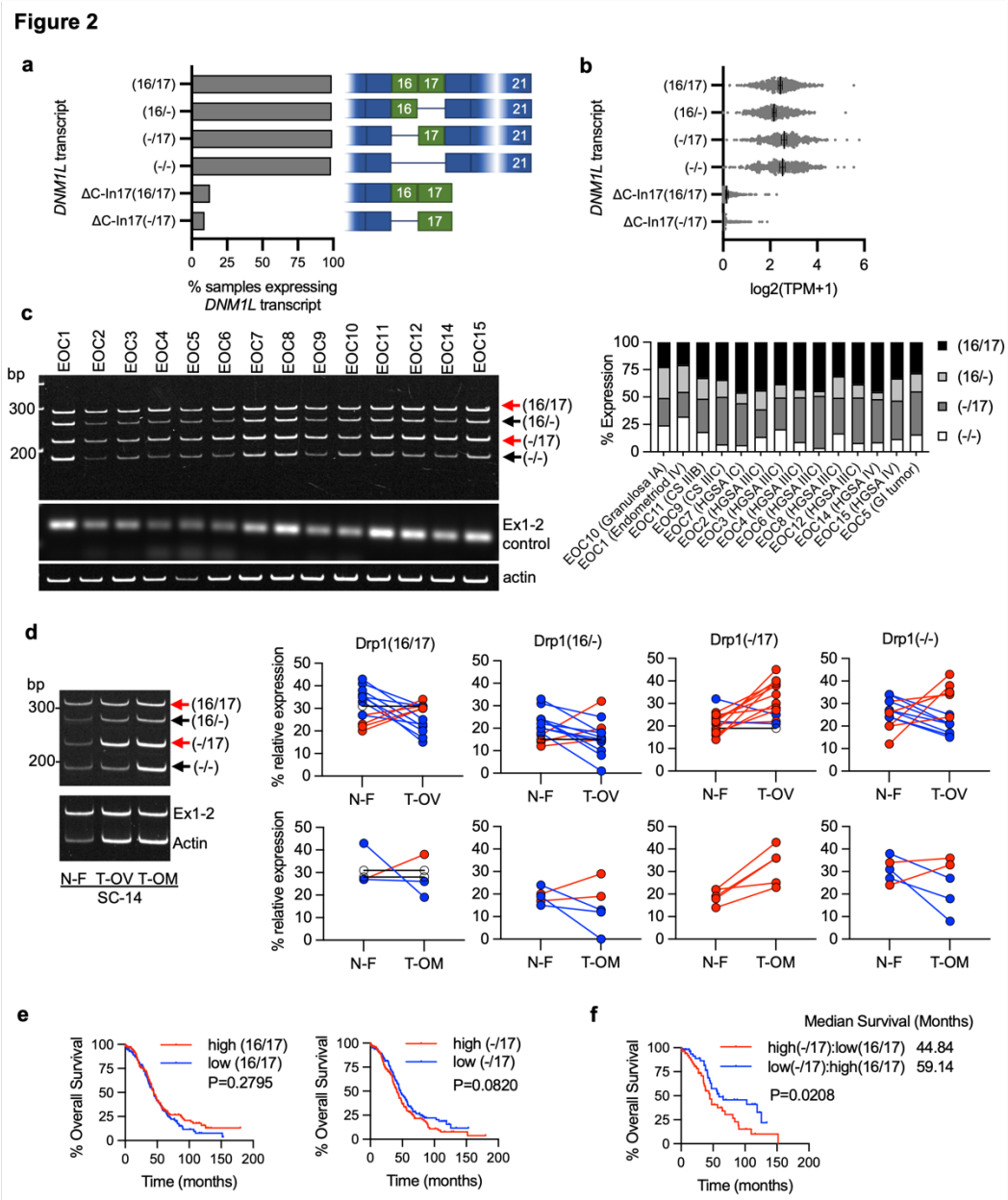

Figure 2. Drp1/*DNM1L* transcript variant expression in ovarian cancer specimens.

a. Frequency of Drp1/*DNM1L* transcript variant expression in Ovarian Serous Cystadenocarcinoma TCGA specimens, focusing on full length variable domain (16/17) transcripts and C terminal truncation terminating in Intron 17 (ΔC-In17). Data represent percentage of specimens displaying TPM values >0.5 for each *DNM1L* transcript variant.

b. Expression levels of *DNM1L* transcript variants from Ovarian Serous Cystadenocarcinoma TCGA data.

c. RT-PCR was used to show relative expression of *DNM1L* variable domain splice variants in a panel of patient ascites derived EOCs. Histologic classification and stage indicated in graph (right; CS: carcinosarcoma; HGSA: high grade serous adenocarcinoma; GI: gastrointestinal).

d. Representative RT-PCR (left) of *DNM1L* variable domain splice variant expression from normal fallopian tube (N-F), and matched ovarian (T-OV) and omental tumors (T-OM).

The relative expression of splice variant transcript Drp1(-/17) is consistently higher in ovarian tumor and omental tumor compared to matched normal fallopian tube specimens (blots see Extended Data Fig. 3; blue lines indicate decreased expression, red lines indicate increased expression, and black lines indicate no change in expression relative to matched normal fallopian tube tissue).

e. Overall survival of TCGA ovarian cancer patients based on DNM1L variant expression. Samples were split at median log2 TPM into high (n=184) and low expression (n=184; log-rank Mantel-Cox test).
f. Overall survival comparison between samples displaying mutually exclusive high Drp1(-/17)/low Drp1(16/17) (n=52) and low Drp1(-/17)/high Drp1(16/17) (n=52) expression (low and high cutoffs based on median log2 TPM; log-rank Mantel-Cox test).

Figure 3

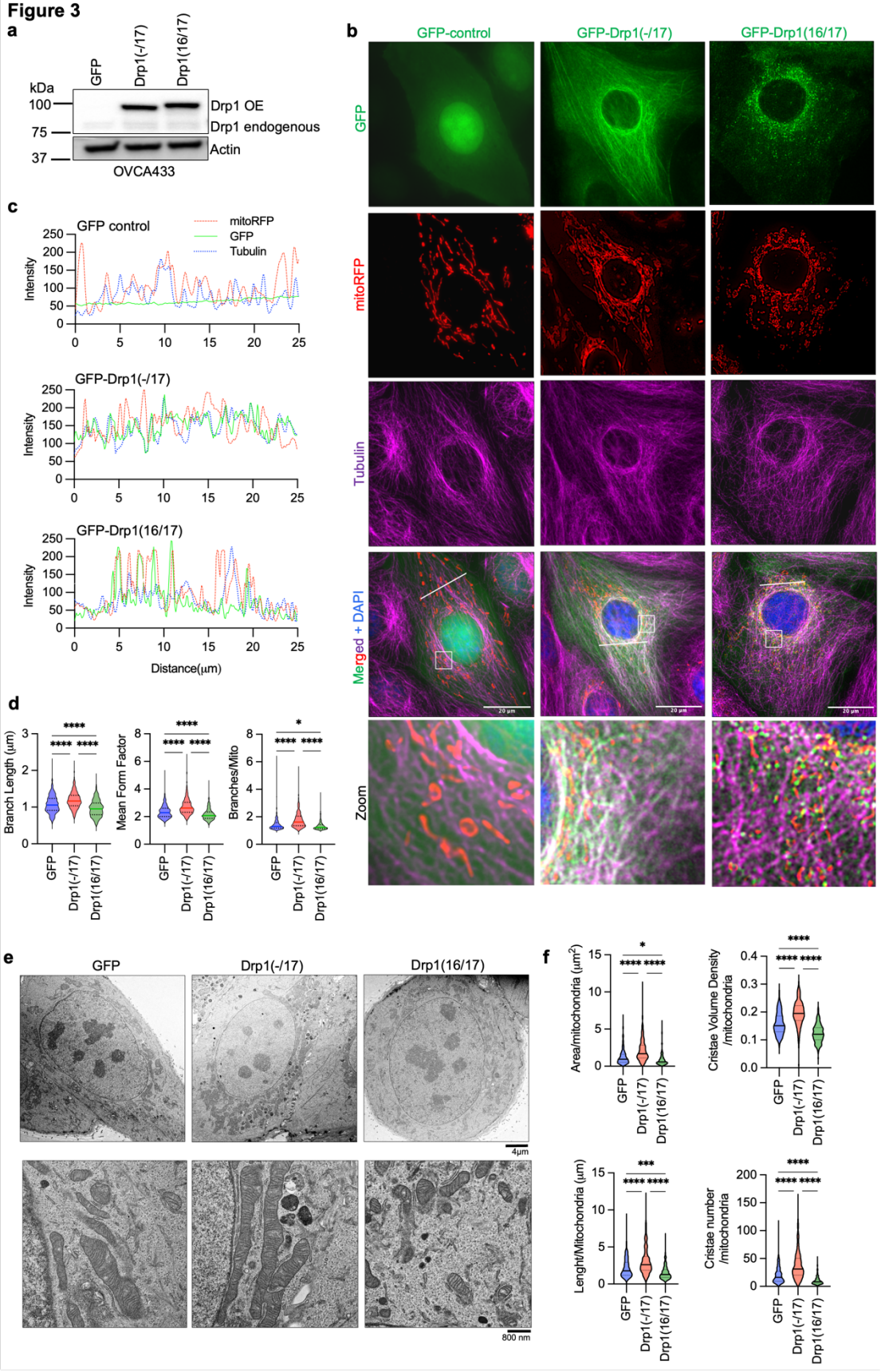

Figure 3. Drp1(-/17) displays decreased association with mitochondria, and its expression increases mitochondrial length and cristae density relative to Drp1(16/17).

a. Western blot analysis of Drp1 expression following transfection of GFP vector control, GFP-tagged Drp1(-/17) or Drp1(16/17) in OVCA433 cells.
b. Representative epifluorescence images of mitochondrial morphology and Drp1 distribution in OVCA433 cells. (Green: GFP or GFP-tagged Drp, Red: mito-RFP to label mitochondria, Magenta: anti-Tubulin antibody and Blue: DAPI). Drp1(-/17) shows a distinct pattern of co-localization with Tubulin, while Drp1(16/17) displays localization to mitochondrial fission puncta. Scale bar: 20 μm.
c. Representative histograms of fluorescence intensity (white line in images on right) illustrate that Drp1(-/17) (green) is more closely aligned with Tubulin (blue) and less so with mitochondria (red). In contrast, GFP-Drp1(16/17) fluorescence peaks coincide with mitochondrial (red) peaks, reflective of association with mitochondrial fission puncta.
d. Drp1(-/17) expressing cells display elongated and branched mitochondrial networks compared to cells expressing Drp1(16/17). Quantification of mitochondrial morphology based on mito-RFP labeling by three independent descriptors (mitochondria analyzer, ImageJ; GFP-control n = 498 cells, Drp1(-/17) n = 568 cells, Drp1(16/17) n=553; one-way ANOVA Mean Form Factor $p < 0.0001$; Branch Length $p < 0.0001$ and Branches/mito $p<0.0001$. Tukey's post test *$p<0.05$, ****$p < 0.0001$).
e. Representative TEM images of OVCA433 cells demonstrate that Drp1(-/17) expressing cells have more fused mitochondria with greater cristae organization and volume compared to cells expressing Drp1(-1/7) or GFP control. Scale bar: 4 μm (upper panels) and 800nm (lower panels).
f. Quantification of mitochondrial morphology and cristae from TEM images (GFP-control n =156 cells, Drp1(-/17) n =160, Drp1(16/17) n=157; one-way ANOVA Area/mitochondria $p<0.0001$, Cristae volume density $p<0.0001$, Length/mitochondria $p<0.0001$ and Cristae number/mitochondria $p<0.0001$. Tukey's post test *$p < 0.05$, ***$p < 0.001$, ****$p < 0.0001$).

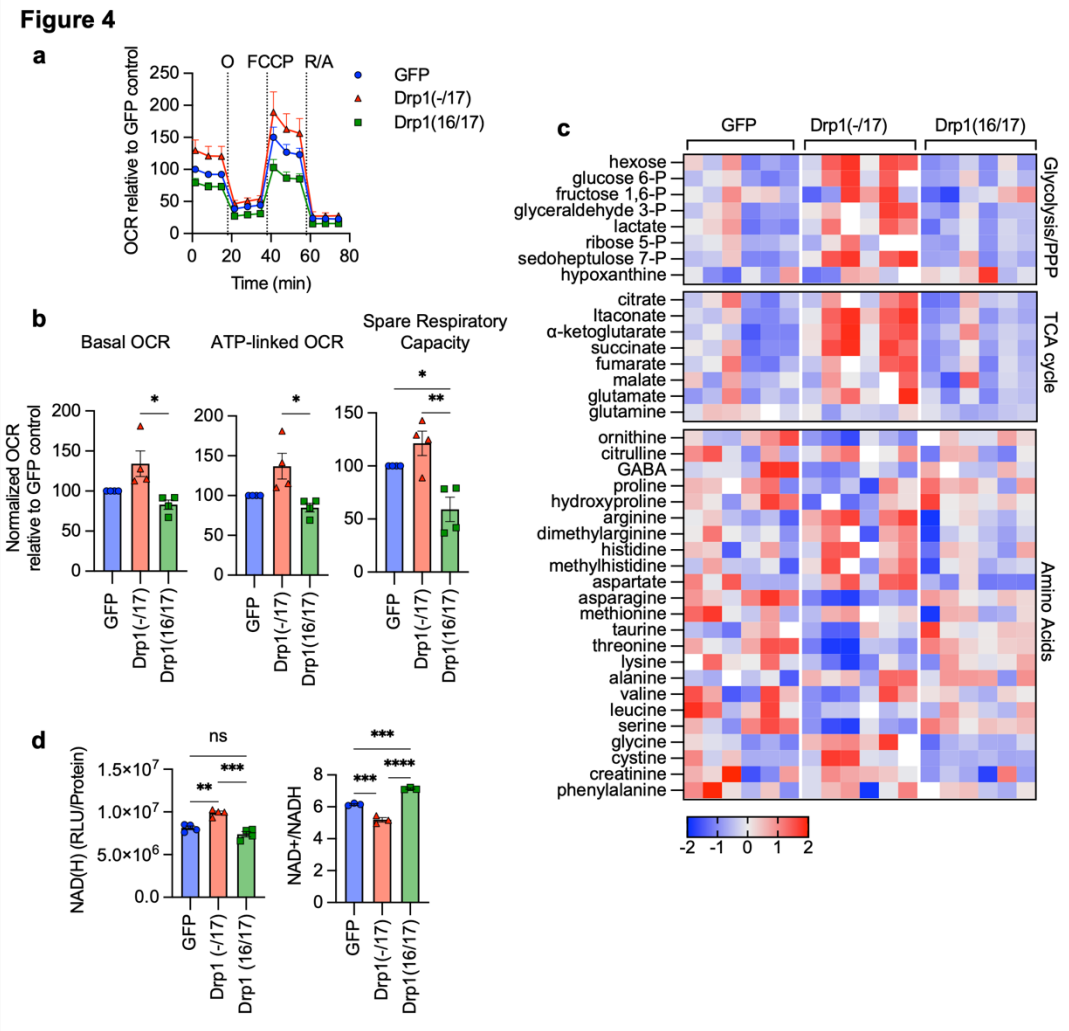

Figure 4. Expression of Drp1(-/17) splice variant increases mitochondrial respiration and TCA cycle metabolites.

a. Expression of Drp1(-/17) increases oxygen consumption rates (OCR) in OVCA433 cells as assessed by Seahorse extracellular flux analysis and the mitochondrial stress test (O: oligomycin A, R/A: rotenone/antimycin A; OCR is normalized to cell viability and expressed relative to GFP control, n=4)

b. Basal OCR, ATP-linked OCR and spare respiratory capacity are increased in OVCA433 cells expressing Drp1(-/17) compared to Drp1(16/17). Data are expressed relative to GFP control (n=4, one-way ANOVA Basal OCR p=0.0144; ATP-linked OCR p=0.0131; spare respiratory capacity p=0.0034; Tukey's post test **p<0.01, ***p<0.001, ****p<0.0001)

c. Relative metabolite content of OVCA433 cells stably expressing GFP control, GFP-Drp1(-/17) or GFP-Drp1(16/17) as assessed by untargeted LC-HRMS (n=6, heatmap reflects z-scores of Area/iSTD values).

d. Total NAD(H) levels are increased in response to Drp1(-/17) expression relative to OVCA433 cells expressing GFP control or Drp1(16/17), while the ratio of NAD+/NADH is significantly decreased (one-way ANOVA NAD(H) n=4, p=0.0002; NAD+/NADH n=3 p<0.0001; Tukey's post test **p<0.01, ***p<0.001, ****p<0.0001).

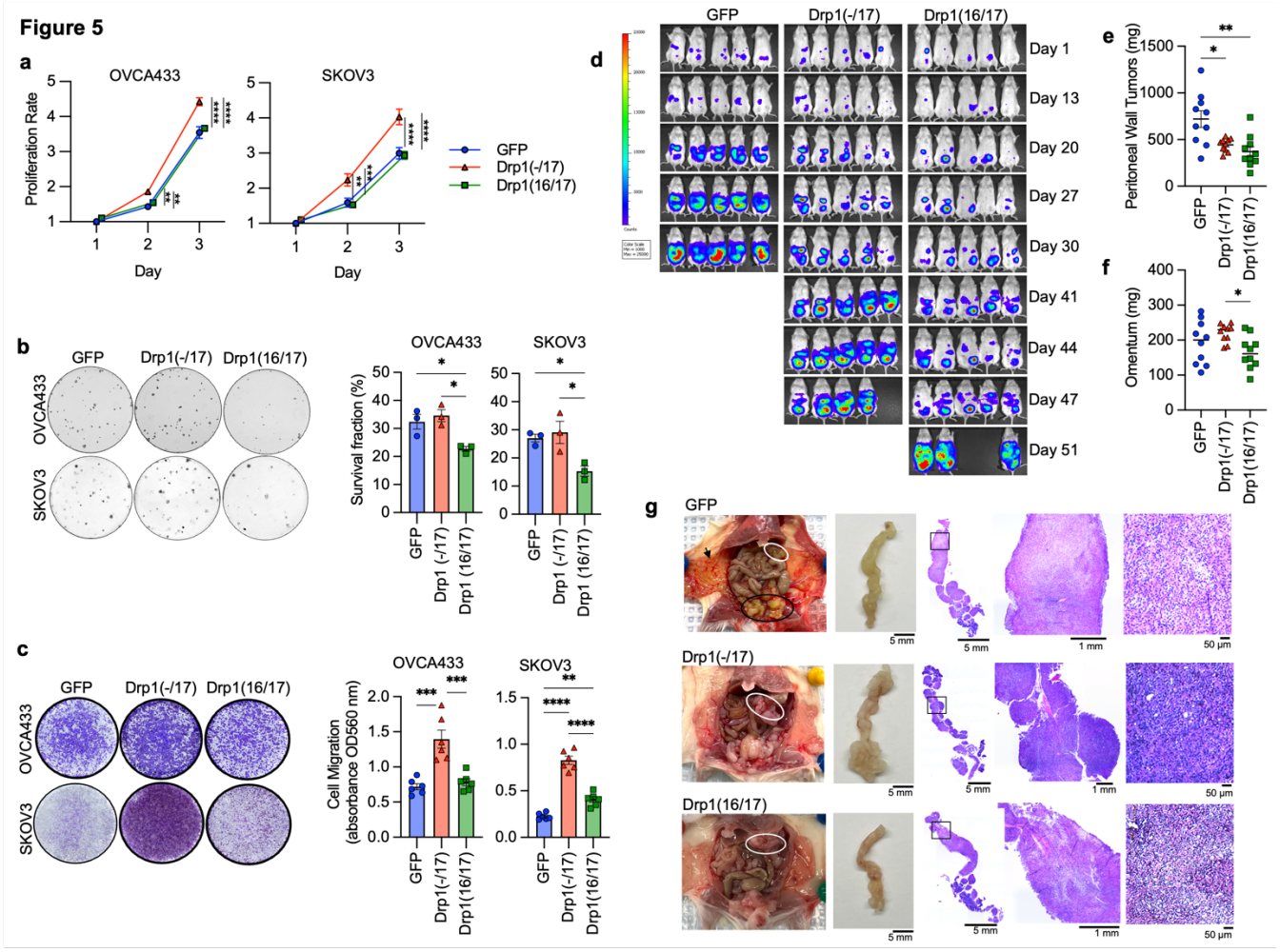

Figure 5. Compared to Drp1(16/17), expression of Drp1(-/17) promotes proliferation and migration, maintains clonogenic survival and drives omental tumor burden of ovarian cancer cells.

a. Drp1(-/17) increases proliferation of OVCA433 and SKOV3 cells. Cell proliferation was assessed by FluoReporter dsDNA quantification, and proliferation rate expressed as increase in the cell density relative to day 1 (n=3, two-way ANOVA group factor variance $p<0.0001$, Tukey's post test $^{**}p<0.01$, $^{***}p<0.001$ and $^{****}p<0.0001$).

b. Drp1(16/17) expression lowers single cell clonogenic survival in both OVCA433 and SKOV3 cells. Cells (100/well) were seeded onto 6-well plates and stained with crystal violet after 7-10 days in culture. Colonies were quantified using ImageJ. Images are representative of 3 independent experiments (n=3, one-way ANOVA OVCA433 $p=0.0128$; SKOV3 $p=0.0201$. Tukey's post test $^{*}p<0.05$).

c. Drp1(-/17) expressing cells are more migratory than Drp1(16/17) or GFP control cells. Cell migration was assessed using the Boyden chamber transwell assay. Images are representative of 3 independent assays (n=3, one-way ANOVA OVCA433 $p=0.0155$; SKOV3 $p=0.0003$. Tukey's post test $^{*}p<0.05$, $^{**}p < 0.01$. and $^{***}p < 0.001$).

d. Peritoneal tumor burden was monitored using bioluminescence imaging at indicated days after NSG mice were injected with $1x10^6$ SKOV3 cells expressing GFP control, Drp1(-/17) or Drp1(16/17) (5 representative mice /group shown).

e. Peritoneal tumor weight was measured after removal at necropsy when mice met endpoints (n=10, median, Kruskal-Wallis P=0.0046, uncorrected Dunn's test *P=0.017).
f. Omental tumor weight was measured after removal at necropsy when mice met endpoints (n=10, median, Kruskal-Wallis P=0.0576, uncorrected Dunn's test *P=0.048, **P=0.0011).
g. Representative image of mice with tumors from SKOV3 cells expressing GFP control, Drp1(-/17) or Drp1(16/17). GFP expressing cells primarily formed peritoneal tumors near the injection site (Black outline) and peritoneal wall (arrow), while Drp1(-/17) expressing cells primarily formed tumors in the omentum (white outline). Gross omental tumors and sectioned omenta followed by H& E staining demonstrate that Drp1(-/17) expressing cells form multiple nodular tumors along the omentum, displacing most of the omental adipocytes.

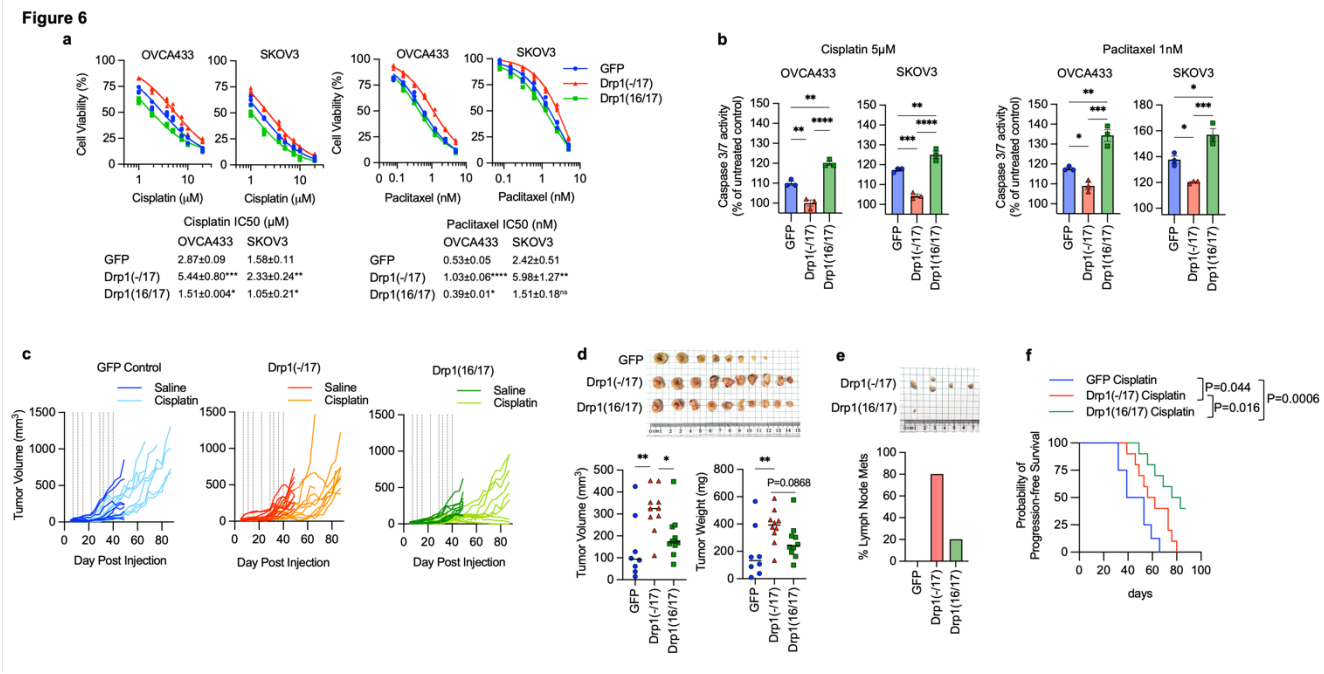

Figure 6. Drp1 splice variant expression affects chemosensitivity of ovarian cancer cells.

a. Expression of Drp1(-/17) decreases sensitivity to cisplatin and paclitaxel. Dose response curves were derived from cell viability assays (FluoReporter dsDNA quantification) of OVCA433 and SKOV3 cells expressing GFP vector control, Drp1(-/17) and Drp1(16/17) in response to cisplatin and paclitaxel treatment (72h). (n=3, one way ANOVA, Dunnet's post test comparison to GFP control *p<0.05, **p<0.01, ***p<0.001, ***p<0.0001).

b. Cells expressing Drp1(-/17) display abrogated apoptosis in response to cisplatin (5 μM) or paclitaxel (1 nM) treatment after 24 hours, as assessed using Caspase-Glo 3/7 assay (n=3, one-way ANOVA cisplatin OVCA433 p=<0.0001, SKOV3 p=<0.0001; paclitaxel OVCA433 p=0.0003, SKOV3 p=0.0006. Tukey's post test *p<0.05, **p<0.01, ***p<0.001, ****p<0.0001).

c. Drp1(16/17) expression leads to Cisplatin sensitivity of SKKOV3 cells in vivo. Subcutaneous tumor growth of SKOV3 cells expressing GFP control, Drp1(-/17) or Drp1(16/17) was monitored following injected into female CrTac:NCr-*Foxn1*^{nu} mice (2 tumors per mouse, n=4-5 mice). Saline or cisplatin (5mg/kg) was administered IP at indicated days (vertical lines on graphs). 4/10 tumors in the Dpr1(16/17) group responded to cisplatin treatment, while all GFP and Drp1(-/17) expressing tumors progressed with treatment.

d. Final tumor volume and weight of SKOV3 subcutaneous tumors from saline treated groups. All mice were euthanized at the same endpoint (day 49; n=8, GPFP; n=10, Drp1(-/17);n=10, Drp1(16/17); median, tumor volume Kruskal-Wallis P=0.0211, uncorrected Dunn's test *P=0.0472, **P=0.0031; tumor weight Kruskal-Wallis P=0.0102, uncorrected Dunn's test **P=0.0062).

e. Drp1(-/17) expressing SKOV3 cells develop lymph node metastases in subcutaneous tumor model. Lymph node metastases were resected in the saline treated groups at day 49 (cisplatin treated group see extended data 10). Graph shows percentage of mice with lymph node metastases.

f. Progression free survival of cisplatin treated mice demonstrates that Drp1(16/17) promotes cisplatin sensitivity of SKOV3 cells. Tumor progression was determined as tumor burden reached volume >200mm^3 (Log-rank Mantel-Cox test).

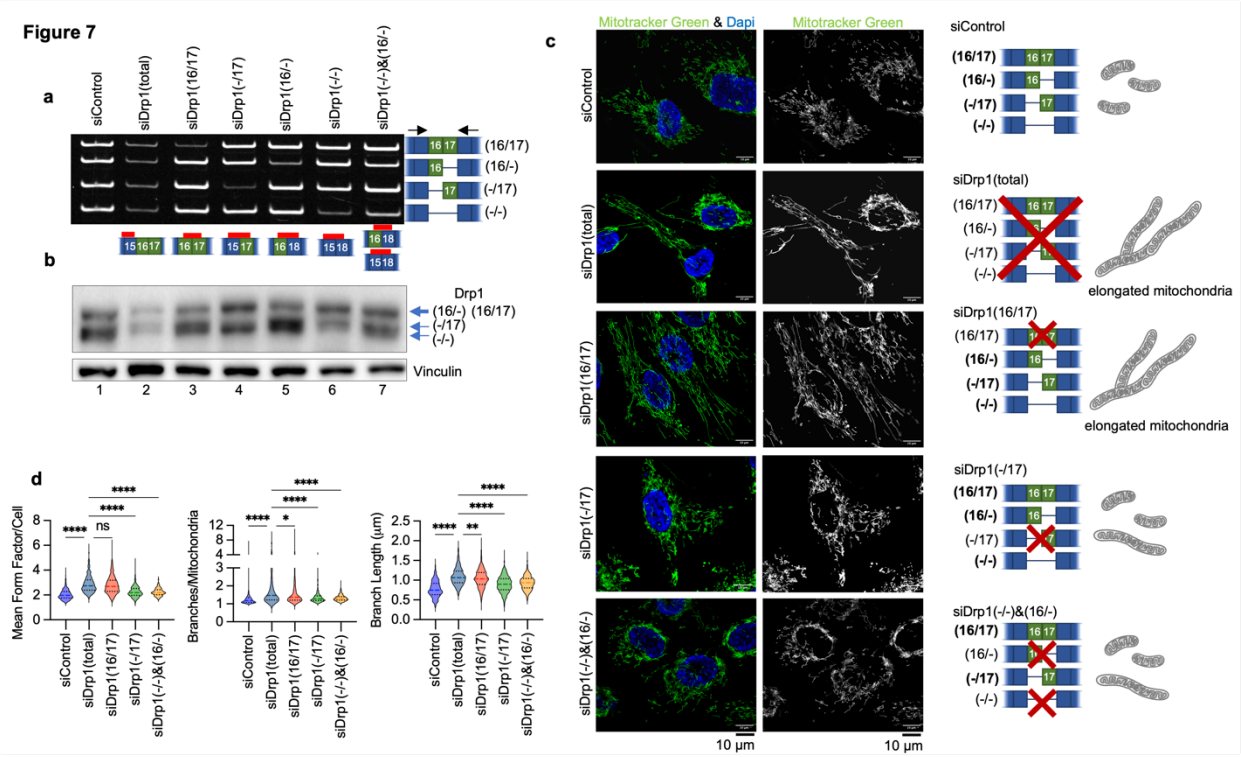

Figure 7. Specific knock-down of endogenous Drp1 splice variants using siRNA and effects on mitochondrial morphology.

a. RT-PCR demonstrating variant specific knock-down of endogenous Drp1 using splice variant specific siRNA in SKOV3 cells. One representative gel from 3 independent replicates shown.
b. Splice variant specific siRNA mediated knock down of Drp1 protein in SKOV3 cells by western blotting. One representative blot from 3 independent replicates shown.
c. Representative epifluorescence images of mitochondrial morphology upon splice variant specific siRNA Drp1 knockdown in SKOV3 cells. (Green: mitotracker green and Blue: DAPI). The disruption of endogenous Drp1 splice variant expression differentially modifies mitochondrial dynamics. siDrp1(16/17) most closely replicates the elongated mitochondrial morphology observed following knock-down of all Drp1 variants (siDrp1 total). Scale bar: 10 µm.
d. Quantification of mitochondrial morphology represented by three independent descriptors as analyzed by mitochondria analyzer (ImageJ, sicontrol n = 560 cells, siDrp1(total) n = 334, siDrp1(16/17) n=630, siDrp1(-/17) n=655, siDrp1(-/-)&(16/-) n=555; one-way ANOVA Mean Form Factor $p < 0.0001$; Branch Length $p < 0.0001$ and Branches/mito $p<0.0001$. Tukey's post test was performed to assess differences between groups and comparisons of groups relative to siDrp1(total) are shown, *$p<0.05$, **$p<0.01$, ****$p < 0.0001$).

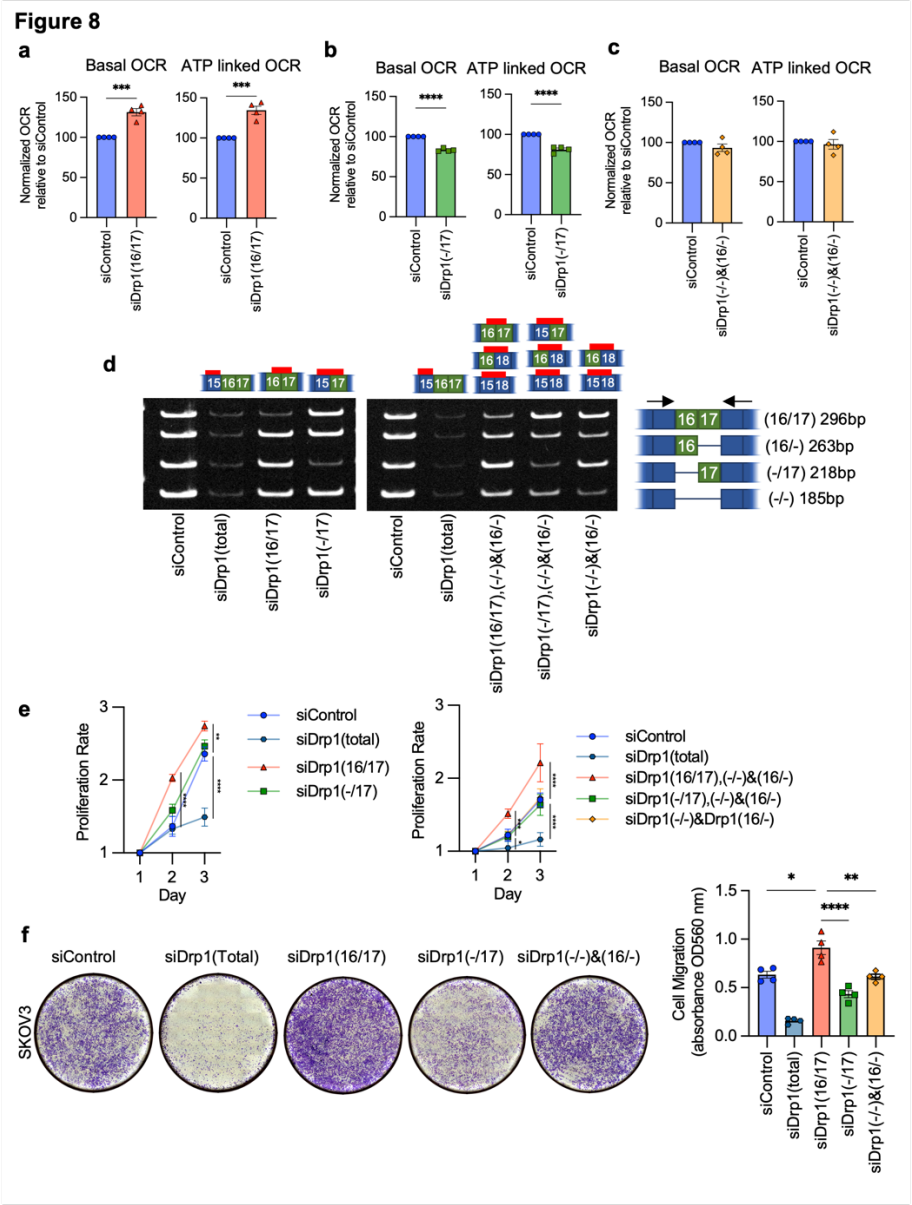

Figure 8. Targeted knock-down of endogenous Drp1 splice variants in SKOV3 cells differentially affect mitochondrial respiration, proliferation and migration.

a. Basal and ATP-dependent oxygen consumption rates (OCR) improved upon siRNA mediated knock down of Drp1(16/17) splice variant,thus increasing the Drp1(-/17):Drp1(16/17) ratio. Mitochondrial respiration was assessed using Seahorse extracellular flux analysis and the mitochondrial stress test (n=4, unpaired t-test. ***p<0.001).
b. Conversely, specific knock down of Drp1(-/17) decreased basal and ATP OCR (n=4, unpaired t-test. ****p<0.0001; OCR: oxygen consumption rate).
c. Mitochondrial respiration remains unchanged when enriching for equal levels of Drp1(-/17) and Drp1(16/17) expression by combination Drp1(16/-) and (Drp1(-/) knock-down (n=4).

d. RT-PCR demonstrating knock-down of Drp1 using single splice variant specific siRNA or combination of siRNAs to enrich for specific Drp1 splice variant expression. One representative gel from independent replicates shown.
e. Single variant knock-down of Drp1(16/17) and Drp1(-/17) variant enrichment with combination knock-down increases proliferation rate of SKOV3 cells relative to siControl. Cell proliferation was assessed by FluoReporter dsDNA quantification and proliferation rate expressed as increase in the cell density relative to day 1. (n=3, two-way ANOVA group factor variance $p<0.0001$, Tukey's post test was performed to assess differences between groups and analysis comparing groups are shown, $*p < 0.05$, $**p < 0.01$, $***p < 0.001$ and $****p < 0.0001$).
f. Endogenous Drp1 splice variants differentially affect cell migration in SKOV3 cells. Knock-down of Drp1(16/17) increases migration, while Drp1(-/17) knock-down reducescell migration relative to siControl cells. After siRNA mediated knock-down, cell migration was assessed using a Boyden chamber transwell assay. Images are representative of 4 independent assays (one-way ANOVA $****p<0.0001$. Tukey's post test was performed to assess differences between groups and analysis comparing siControl, siDrp1(16/17), siDrp1(-/17) and siDrp1(-/-)&(16/-) groups are shown, Tukey's multiple comparison $*p<0.05$, $**p < 0.01$. and $****p < 0.0001$).

Extended Data Figures:

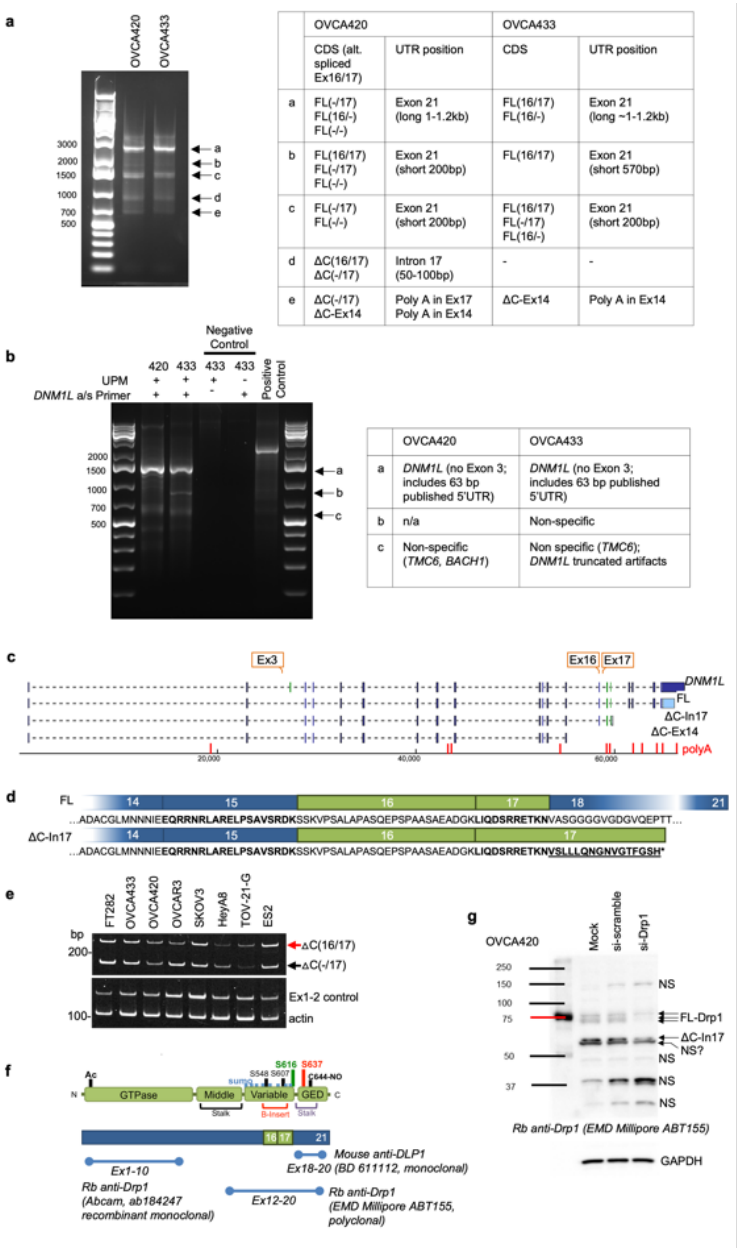

	OVCA420		OVCA433	
	CDS (alt. spliced Ex16/17)	UTR position	CDS	UTR position
a	FL(-/17) FL(16/-) FL(-/-)	Exon 21 (long 1-1.2kb)	FL(16/17) FL(16/-)	Exon 21 (long ~1-1.2kb)
b	FL(16/17) FL(-/17) FL(-/-)	Exon 21 (short 200bp)	FL(16/17)	Exon 21 (short 570bp)
c	FL(-/17) FL(-/-)	Exon 21 (short 200bp)	FL(16/17) FL(-/17) FL(16/-)	Exon 21 (short 200bp)
d	ΔC(16/17) ΔC(-/17)	Intron 17 (50-100bp)	-	-
e	ΔC(-/17) ΔC-Ex14	Poly A in Ex17 Poly A in Ex14	ΔC-Ex14	Poly A in Ex14

	OVCA420	OVCA433
a	*DNM1L* (no Exon 3; includes 63 bp published 5'UTR)	*DNM1L* (no Exon 3; includes 63 bp published 5'UTR)
b	n/a	Non-specific
c	Non-specific (*TMC6, BACH1*)	Non specific (*TMC6*); *DNM1L* truncated artifacts

Extended Data Figure 1. Identification of Drp1 transcript variants in ovarian cancer cell lines.

a. 3' RACE reveals that ovarian cancer cell lines OVCA420 and OVCA433 express multiple Drp1/*DNM1L* transcripts variants, including full length (FL) transcripts with alternatively spliced exons 16 and 17, and C terminal truncated transcripts at exon 14 (ΔC-Ex14) and intron 17 (ΔC-In17). 3' RACE was carried out using SMARTer 3'5'RACE kit (Takara). PCR products from each cell line (a-e) were gel-extracted and cloned into the in-Fusion pRACE vector. 3-5 colonies per clone were selected for sequencing to determine the major5'RACE products in OVCA420 and OVCA433 cells (Table).

b. 5’ RACE reveals that *DNM1L* transcripts expressed in OVCA420 and OVCA433 cell share the same 5’UTR and lack exon 3. 5’ RACE was carried out using SMARTer 3’RACE kit (Takara) the with the Universal Primer A Mix (UPM) and the *DNM1L* specific antisense primer, positioned in Exon 12. PCR products from each cell line (a-c) were gel-extracted and cloned into the in-Fusion pRACE vector. 3-5 colonies per clone were selected for sequencing to determine the major 5’RACE products in OVCA420 and OVCA433 cells (Table).
c. Transcript variants identified in OVCA420 and OVCA433 cells include alternative splicing of the variable domain exons 16 and 17; variable lengths of 3’UTRs, and utilization of proximal polyadenylation, resulting in two C terminal truncation variants, terminating in Intron 17 (ΔC-In17) and exon 14 (ΔC-Ex14; indicated in red; PolyA_DB v.3.2; PolyASites). 5’RACE demonstrated that ovarian cancer cell lines cell share the same 5’UTR and lack exon 3.
d. Schematic of the *DNM1L* variable domain Exons 16 and 17 alternatively spliced in ovarian cancer cells and corresponding amino acid sequences. The variant terminating in Intron 17 (ΔC-In17) also displays variable domain exon 16 alternative splicing and is predicted to encode an additional 16 amino acids from the adjacent intron to terminate at an alternate STOP codon.
e. RT-PCR with primers designed to detect the intronic retention of the 3’ region of ΔC-In17 illustrates that the *DNM1L* C terminal truncation variant terminating in Intron 17 can be detected in most ovarian cancer cell lines to variable degrees and that these transcripts can vary in their splicing of exon 16.
f. Position of epitopes used to generate commercially available Drp1 antibodies. Note that C-terminal targeted antibody BD611112 is predicted not to recognize potential C-terminal truncations.
g. Protein variants identified in the range of 65-80kDa by western are verified to be Drp1 by siRNA mediated knock-down. Non-specific bands (n/s) are not affected by siRNA against Drp1.

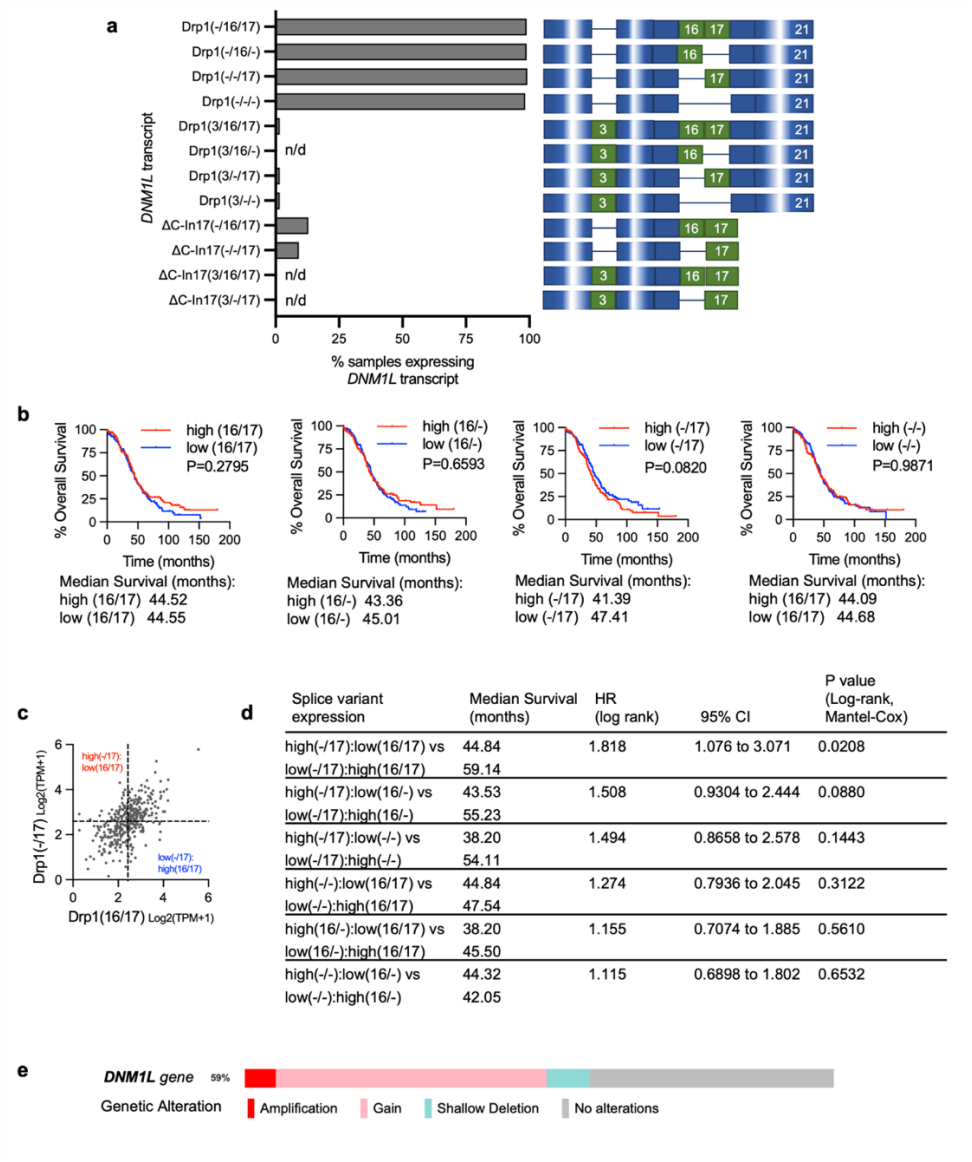

Splice variant expression	Median Survival (months)	HR (log rank)	95% CI	P value (Log-rank, Mantel-Cox)
high(-/17):low(16/17) vs low(-/17):high(16/17)	44.84 59.14	1.818	1.076 to 3.071	0.0208
high(-/17):low(16/-) vs low(-/17):high(16/-)	43.53 55.23	1.508	0.9304 to 2.444	0.0880
high(-/17):low(-/-) vs low(-/17):high(-/-)	38.20 54.11	1.494	0.8658 to 2.578	0.1443
high(-/-):low(16/17) vs low(-/-):high(16/17)	44.84 47.54	1.274	0.7936 to 2.045	0.3122
high(16/-):low(16/17) vs low(16/-):high(16/17)	38.20 45.50	1.155	0.7074 to 1.885	0.5610
high(-/-):low(16/-) vs low(-/-):high(16/-)	44.32 42.05	1.115	0.6898 to 1.802	0.6532

Extended Data Figure 2. Drp1/*DNM1L* transcript variant expression in ovarian cancer specimens from TCGA.

a. Frequency of Drp1/*DNM1L* transcript variant expression, focusing on full length transcpri variants and alternatively spliced exons 3, 16 and 17 (3/16/17) transcripts and C terminal truncation terminating in Intron 17 (ΔC-In17). Dash denotes exon is spliced out. Data represent percentage of specimens displaying log2 TPM+1 values >0.5 for each DNM1L variant.

b. Overall survival of TCGA patients based on DNM1L variant expression. Samples were split at median log2 TPM into high (n=184) and low expression (n=184; log-rank Mantel-Cox test).

c. Drp1(-/17) expression relative to Drp1(16/17; log2 TPM+1). Mutually exclusive high and low expression of variant pairs is based on median log2 TPM+1 expression cut offs indicated by dotted line.

d. Overall survival data of TCGA ovarian cancer patients grouped into mutually exclusive high/low expression of Drp1 transcript variant pairs. Low and high cutoffs based on median expression. Patients with high Drp1(-/17) and low Drp1(16/17) expression display significantly decreased overall survival compared to patients with high Drp1(16/17) and low Drp1(-/17) transcript levels in their tumors.
e. *DNM1L* gene copy number alterations in 233 Ovarian Serous Cystadenocarcinoma cases with complete CNA data (TCGA, PanCancer Atlas). 5% of cases display high level amplification, 46% low level gain, and 7% shallow deletion.

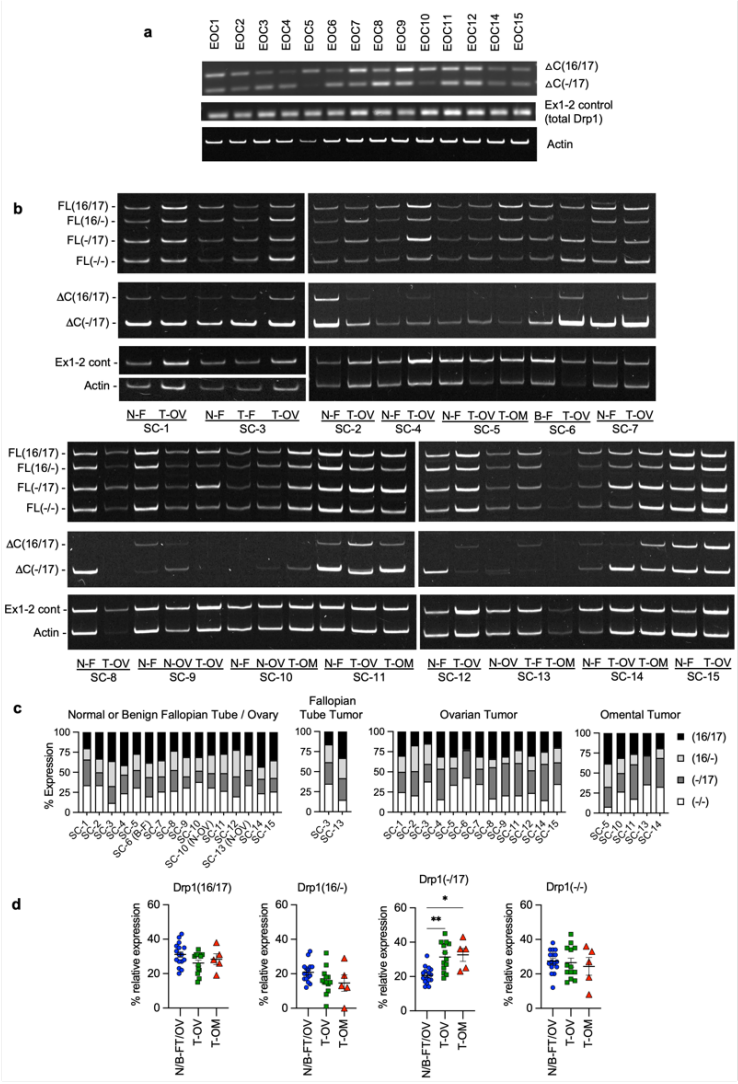

Extended Data Figure 3. Expression of DNM1L splice variants in matched patient specimens.

a. RT-PCR was used to show relative expression of ΔC(-/17) and ΔC(16/17) truncated transcripts of DNM1L in a panel of patient ascites derived EOCs. (EOC9 & 11: carcinosarcoma; EOC 2,3,4 HGSA high grade serous adenocarcinoma; GI: gastrointestinal; tumor stage is indicated in Figure 2c).
b. RT-PCR of *DNM1L* variable domain splice variant expression from normal fallopian tube (N-F), and matched ovarian (T-OV) and omental tumors (T-OM). The relative expression of splice variant transcript Drp1(-/17) is consistently higher in ovarian tumor and omental tumor compared to matched normal fallopian tube specimens N=normal, T=tumor, B=benign, F=fallopian tube, OV= ovary, OM= omentum. All specimens were classified as HGSA, and the following stage: SC-1: IIIC, SC-2: IIIB, SC-3: IIIC, SC-4: IB, SC-5: IIIC, SC-6: IC3, SC-7: IIIB, SC-8: IIIC, SC-9: IVB, SC-10: IIIC, SC-11: IIIB, SC-12: IC2, SC-13: IIIC, SC-14: IIIC, SC-15: IIIB.
c. Quantification of relative Drp1 variable domain splice variant expression from panel b.
d. Comparison of relative expression of each variant between normal fallopian tube/ovary and ovarian tumor or omental tumor. Relative expression of Drp1(-/17) compared to

other variants is significantly increased in ovarian tumors and omental tumors compared to matched normal tissues. (Mixed Effects Analysis with Tukey's post test. *p<0.05, **p<0.01).

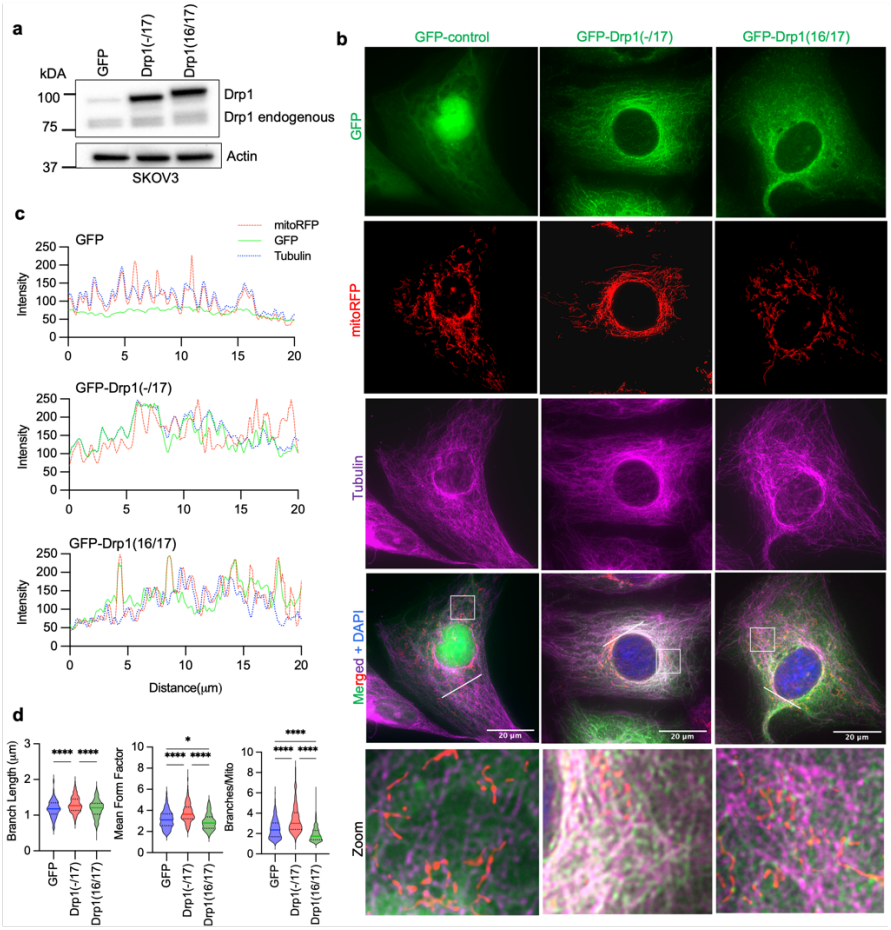

Extended Data Figure 4: Drp1(-/17) displays decreased association with mitochondria and increased localization to microtubules in SKOV3 cells.

a. Western blot analysis of Drp1 expression following transfection of GFP vector control, GFP-tagged Drp1(-/17) or Drp1(16/17) in SKOV3 cells.
b. Representative epifluorescence images of mitochondrial morphology and Drp1 distribution in SKOV3 cells. (Green: GFP or GFP-tagged Drp, Red: mito-RFP to label mitochondria, Magenta: anti-Tubulin antibody and Blue: DAPI). Drp1(-/17) expression is strongly co-localized with Tubulin while Drp1(16/17) localizes to mitochondrial fission puncta. Scale bar: 20 µm.
c. Representative histograms of fluorescence intensity (white line in images on right) illustrate that Drp1(-/17) (green) is more closely aligned with Tubulin (blue) and less so with mitochondria (red) in SKOV3 cells. In contrast, GFP-Drp1(16/17) fluorescence peaks coincide with mitochondrial (red) peaks, reflective of association with mitochondrial fission puncta.
d. Drp1(-/17) expressing SKOV3 cells display elongated and branched mitochondrial networks compared to cells expressing Drp1(16/17). Quantification of mitochondrial morphological was carried out using mitochondria analyzer in ImageJ. (GFP-control n = 180 cells, Drp1(-/17) n = 224 cells, Drp1(16/17) n=252 cells one-way ANOVA Mean

Form Factor p <0.0001; Branch Length p <0.0001; Branches/mito p <0.0001. Tukey's post test *p<0.05, ****p <0.0001).

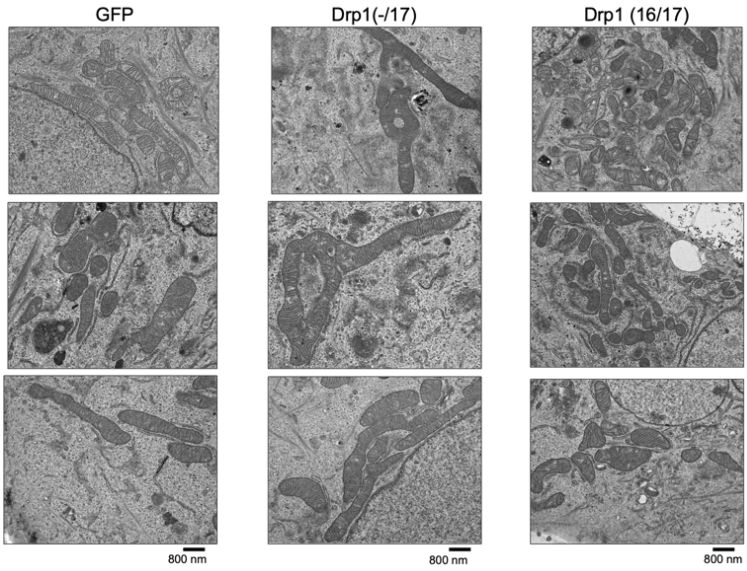

Extended Data Figure 5: Drp1(-17) and Drp1(16/17) expression differentially alter mitochondrial architecture of OVCA433 cells.

Representative TEM images from 3 individual biological replicates demonstrate a more fused mitochondrial morphology in Drp1(-/17) cells compared to the smaller, fragmented mitochondria characteristic of Drp1(16/17) cells.

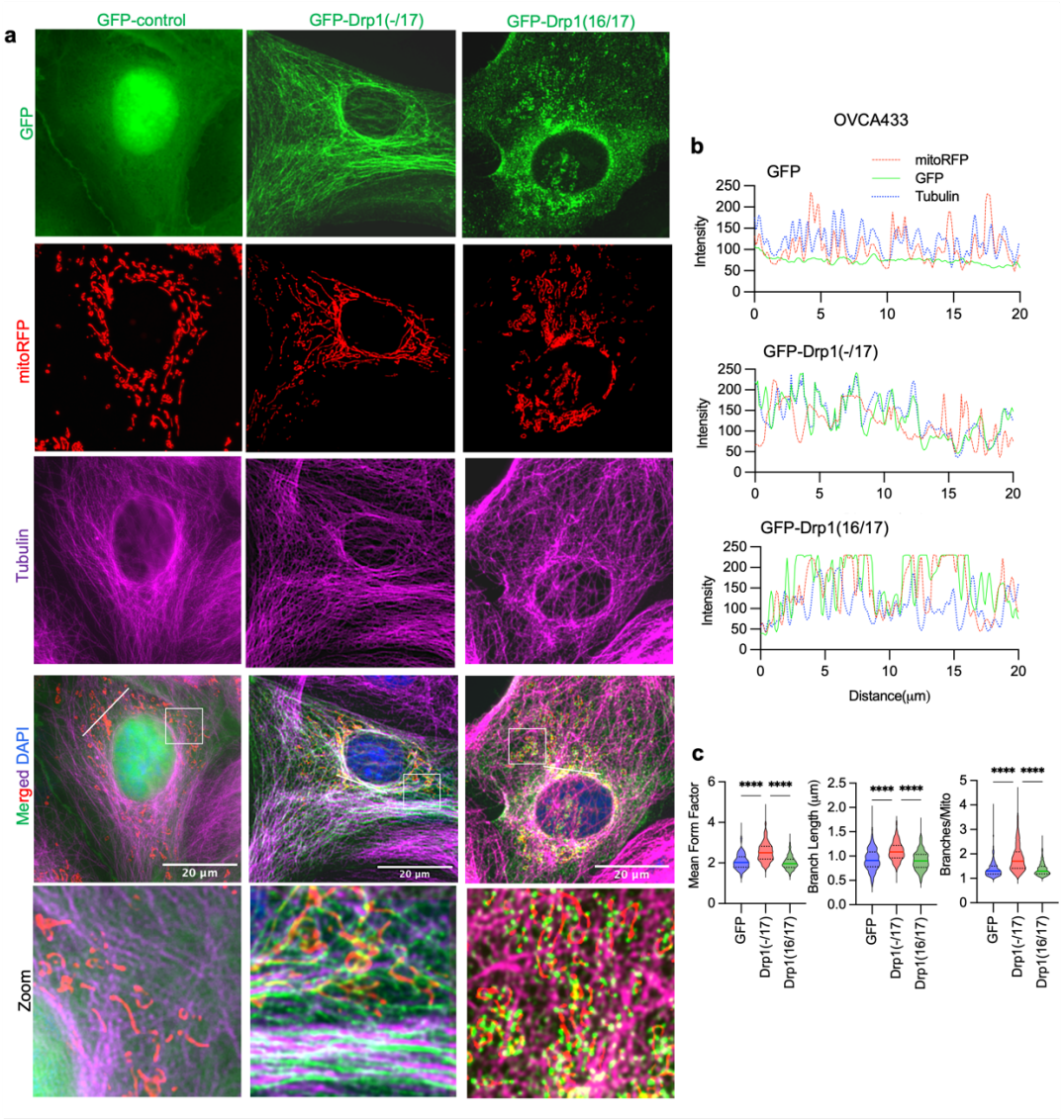

Extended Data Figure 6. Drp1(-/17) displays decreased association with mitochondria in response to FCCP.

a. Drp1(-/17) preserves its localization with Tubulin upon treatment with the fission stimulus FCCP. In contrast, Drp1(16/17) associates with fission puncta at mitochondria in response to FCCP. Representative epifluorescence images are shown of mitochondrial morphology and Drp1 distribution after 30 minutes with FCCP treatment (1μM) in OVCA433 cells. (Green: GFP or GFP-tagged Drp1, Red: mitochondria targeted RFP, Magenta: anti-Tubulin, Blue: DAPI; Scale bar: 20 μm).

b. Representative histogram of fluorescence intensity of GFP-Drp1 (green) in conjunction with mitochondria (red) and Tubulin (blue), illustrates that GFP-Drp1(16/17) strongly overlaps with mitochondria following FCCP treatment (1 μM, 30 mins). Conversely, Drp1(-/17) continues to show overlapping localization with tubulin rather than mitochondria.

c. OVCA433 cells expressing Drp1(16/17) or GFP control display decreased mitochondrial length and increased fragmentation compared to cells expressing Drp1(-/17) in response

to FCCP. Quantification of mitochondrial morphological represented by three independent descriptors as analyzed by mitochondria analyzer in ImageJ. n = 301 cells from GFP-control, n = 285 cells from Drp1(-/17) and n=287 from Drp1(16/17) were analyzed. (one-way ANOVA Mean Form Factor $p < 0.0001$; Branch Length $p < 0.0001$ and Branches/mito $p<0.0001$. Tukey's post test $*p<0.05$, $****p < 0.0001$).

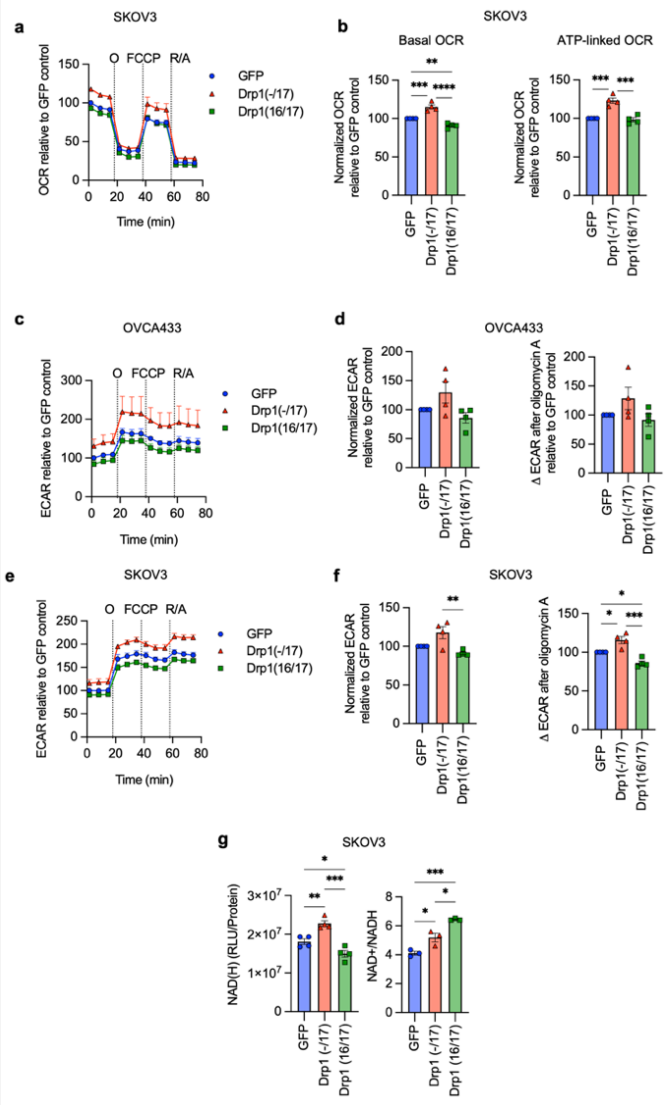

Extended Data Figure 7. Expression of Drp1(-/17) splice variant increases mitochondrial respiration in SKOV3 cells.

a. Expression of Drp1(-/17) increases oxygen consumption rates (OCR) in SKOV3 cells as assessed by Seahorse extracellular flux analysis and mitochondrial stress test (O: oligomycin A, R/A: rotenone/antimycin A; OCR is normalized to cell viability and expressed relative to GFP control, n=4)

b. Basal OCR and ATP-linked OCR are increased in SKOV3 cells expressing Drp1(-/17) compared to Drp1(16/17). Data are expressed relative to GFP control (n=4, one-way ANOVA Basal OCR $p<0.0001$; ATP-linked OCR $p=0.0001$; Tukey's post test $^{*}p<0.05$, $^{**}p<0.01$)

c. ECAR traces derived from the mitochondrial stress test (Fig 4A) of OVCA433 cells expressing GFP control, Drp1(-/17) or Drp1(16/17).

d. Basal ECAR and ΔECAR following oligomycin A inhibition of ATP-synthase were quantified in OVCA433 cells expressing GFP control, Drp1(-/17) or Drp1(16/17) (n=4, one-way ANOVA Basal ECAR p=0.0743; ΔECAR p=0.1501).
e. Extracellular acidification rates (ECAR) of SKOV3 cells expressing GFP control, Drp1(-/17) or Drp1(16/17). ECAR traces are derived in parallel to OCR values from mitochondrial stress test.
f. Basal ECAR and ΔECAR following oligomycin A inhibition of ATP-synthase were quantified in SKOV3 cells expressing GFP control, Drp1(-/17) or Drp1(16/17) (n=4, one-way ANOVA Basal ECAR p=0.0088; ΔECAR p=0.0003; Tukey's post test *p<0.05, **p<0.01, ***p<0.001).
g. Total NAD(H) levels are increased in response to Drp1(-/17) expression relative to SKOV3 cells expressing GFP control or Drp1(16/17), while the ratio of NAD+/NADH is significantly decreased (one-way ANOVA NAD(H) n=4, p=0.0002; NAD+/NADH n=3 p=0.0004; Tukey's post test *p<0.05, ***p<0.001, ****p<0.0001).

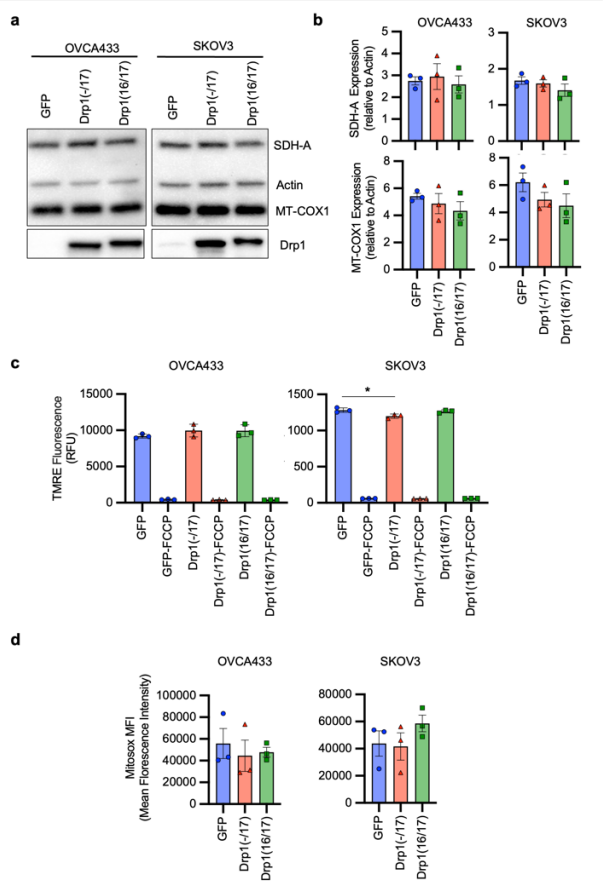

Extended Data Figure 8. Expression of Drp1 (-/17) or Drp1(16/17) does not affect protein levels of ETC components or mitochondrial membrane potential in ovarian cancer cells.

a. Levels of nuclear-DNA encoded SDH-A (Complex II) and mitochondrial-DNA encoded COX-1 (Complex IV) proteins are unchanged in both Drp1(-/17) and Drp1(16/17) expressing cells compared to GFP control cells. Data from one experimental replicate western blot is shown.
b. Quantification of SDH-A and MT-COX1 protein expression normalized to β-Actin in OVCA433 and SKOV3 cells by densitometry using ImageJ. (n=3, one-way ANOVA SDH-A expression; OVCA433 p=0.8407, SKOV3 p=0.3893, MT-COX1 expression; OVCA333 p=0. 4876, SKOV3 p=0. 2842).
c. Mitochondrial membrane potential was measured using TMRE (100nM) at baseline and with FCCP treatment (10 μM, 30 mins) in OVCA433 and SKOV3 cells expressing GFP control, Drp1(-/17) or Drp1(16/17) (n=3, one-way ANOVA of untreated cells OVCA433 p=0.3908, SKOV3 p=,0.0256, Tukey's post test *p=0.0264; one-way ANOVA comparison of FCCP treated cells OVCA433 p=0.3449, SKOV3 p=0.1715).
d. Drp1(-/17) and Drp1(16/17) overexpression in OVCA433 and SKOV3 cells did not alter MitoSox fluorescence, a mitochondrial targeted dye susceptible to superoxide mediated oxidation (n=3, one-way ANOVA OVCA433 p=0.7971, SKOV3=0.3830).

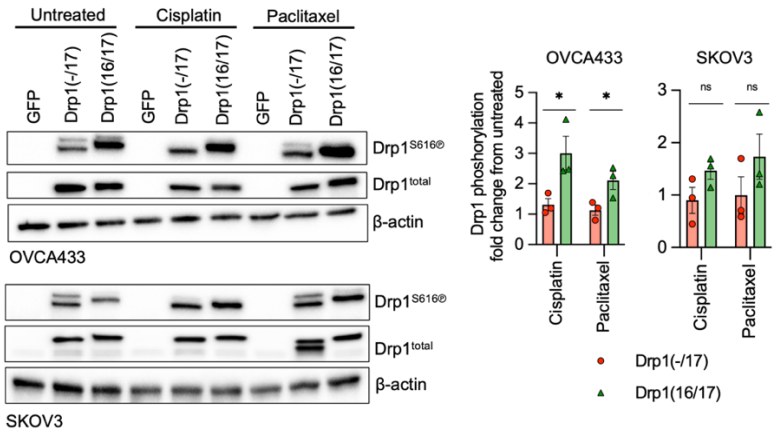

Extended Data Figure 9. S616 phosphorylation of recombinant expressed Drp1 following cisplatin and paclitaxel treatment, as assessed by western blotting.

Changes in Drp1 phosphorylation (S616) in response to cisplatin (5 μM) and paclitaxel (1 nM) was assessed using western blotting (Densitometry quantification was carried out using ImageJ and normalizing to total Drp1, data are expressed relative to untreated control, n=3, unpaired t test *p<0.05).

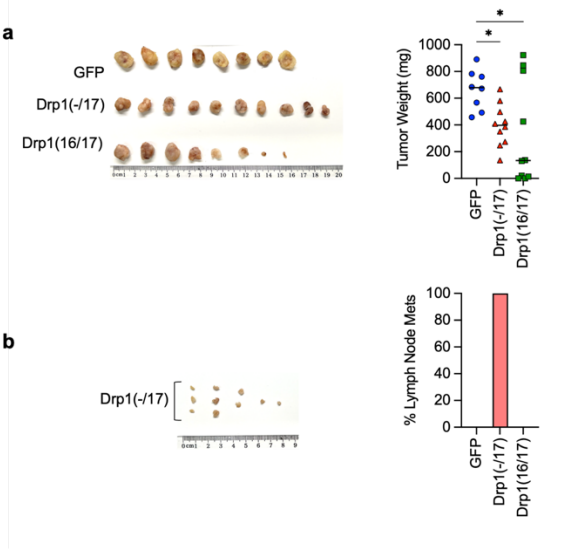

Extended Data Figure 10. Tumor morphology and lymph node metastases after Cisplatin treatment. Drp1(-/17) expression leads to gross difference in tumor morphology and lymph node metastasis in cisplatin treated groups.

a. Final tumor weight of SKOV3 subcutaneous tumors from cisplatin treated groups as mice reached endpoints; n=8, GFP; n=10, Drp1(-/17); n=10, Drp1(16/17); median shown, Kruskal-Wallis P=0.0377 uncorrected Dunn's test *P<0.05).
b. Mice injected with Drp1(-/17) expressing SKOV3 cells were the only group that develop lymph node metastases in the subcutaneous tumor model under cisplatin treatment. Lymph node metastases were resected as mice reached endpoints. Graph shows percentage of mice with lymph node metastases.

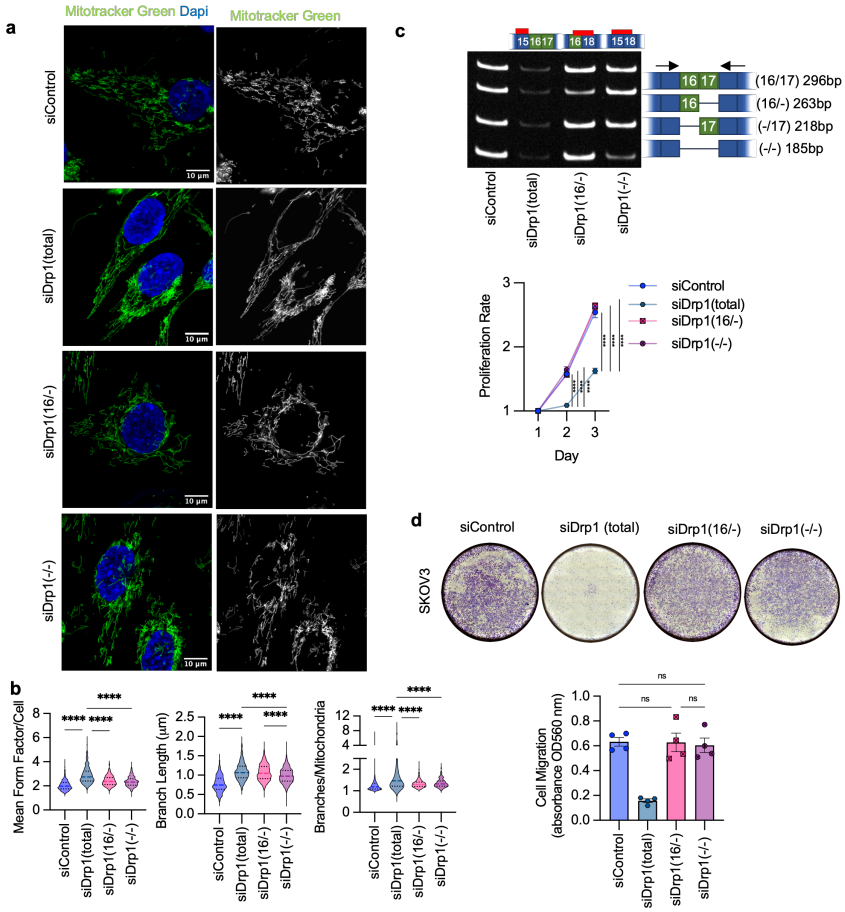

Extended Data Figure 11. Specific knock-down of endogenous Drp1(-/-) and Drp1(16/-) variants and effects on mitochondrial morphology, cell proliferation and migration.

a. Representative epifluorescence images of mitochondrial morphology upon splice variant specific siRNA Drp1 knockdown in SKOV3 cells. (Green: mitochondria stained with mitotracker green and Blue: DAPI). Scale bar: 10 µm.

b. Quantification of mitochondrial morphological represented by three independent descriptors as analyzed by mitochondria analyzer in ImageJ. (n = 560 cells siControl, n = 334 cells siDrp1(total), n=630 siDrp1(16/17), n=655 siDrp1(-/17), n=555 siDrp1(-/-)&(16/-); one-way ANOVA Mean Form Factor p <0.0001; Branch Length p <0.0001 and Branches/mito p<0.0001. Tukey's post test was performed to assess differences between groups and analysis comparing groups to siDrp1(total) are shown, ****p <0.0001).

c. Individual Drp1(-/-) and Drp1(16/-) variant specific knockdown did not alter cell proliferation in SKOV3 cells as no difference in proliferation rate compared to siControl cells. Cell proliferation was assessed by FluoReporter dsDNA quantification and proliferation rate expressed as increase in the cell density relative to day 1 (n=4, two-way ANOVA group factor variance p<0.0001, Tukey's post test ****p < 0.0001).

d. Cell migration was unchanged upon knock-down of either Drp1(-/-) or Drp1(16/-) splice variant in SKOV3 cells. Post Drp1 knock-down, cell migration was assessed using the Boyden chamber transwell assay and quantified by measuring the absorbance of the crystal violet staining of migrated cells. Images are representative of 4 independent assays (n=4, one-way ANOVA ****p<0.0001. Tukey's post test was performed to assess

differences between groups and analysis comparing siControl, siDrp1(16/17), siDrp1(-/17) and siDrp1(-/-)&(16/-) groups are shown).